# Behaviour of embedded H-profile balcony-to-slab connection

Piseth Heng, Hong Hanh Le, Hugues Somja, Franck Palas, Clemence Lepourry-Nicollet

# Behaviour of embedded H-profile balcony-to-slab connection

Piseth Heng[a,*], Hong Hanh Le[a], Hugues Somja[a], Franck Palas[b], Clemence Lepourry-Nicollet[a,c]

[a] *INSA Rennes, LGCGM/ Structural Engineering Research Group, 20 avenue des Buttes de Coësmes, CS 70839, F-35708 Rennes Cedex 7, France*

[b] *Concept Technique Design R & D, 89 Boulevard de Laval, 35500 Vitré, France*

[c] *Ingenova, Civil Engineering Office, 5 Rue Louis Jacques Daguerre, Saint Jacques de la Lande 35136, France*

*Corresponding author: piseth.heng@insa-rennes.fr

## Abstract

This paper investigates experimentally and numerically the behaviour of a balcony-to-slab connection made by an H-profile embedded in the concrete slab. A large-scale test was performed on a specimen of the connection system in order to determine the moment-bearing capacity, the deformation behaviour, the cracking patterns, the distribution of the bending moment along the axis of the embedded steel H-profile as well as the failure mode of the connection system. The test results showed that the failure mode was governed by the concrete shear of the slab. In addition, a 3D finite element model of the experimental test was also carried out and successfully validated against the experimental results. For a practical design of the connection system, a model based on Timoshenko beam on elastic foundation (BEF) was investigated and verified against the results obtained from the validated FE model. The Winkler modulus of the BEF model was determined by considering the local deformation of the concrete based on a strut-and-tie model. The results demonstrate that the BEF model with this value of the Winkler modulus provides a conservative estimation of the shear and bending forces applied to both the embedded H-profile and the concrete cross-sections. This method is a first tentative design basis using linear elastic theory for such a system.

*Keywords:* Embedded H-profile, Timoshenko beam on elastic support, Winkler modulus, Large-scale test, FE simulation.

## 1. Introduction

The technique of embedding steel profiles in concrete has been used as a connection between structural steel, reinforced concrete, and composite elements for years for its high ductility, compactness and simplicity of detailing. The application of the embedded steel profile in precast concrete columns as a replacement of reinforced concrete corbels or brackets can be traced back to the 1970s [1]-[4]. Based on calibrations against experimental data, different analytical design methods were proposed in these researches by adopting assumptions on the distributions of bearing stress over the profile flange and along the embedded length. Mattock and Gaafar [4] assumed a parabolic distribution (see Figure 1) for the compressive stresses in the concrete above the embedded section and a uniform distribution for the compressive stresses below the embedded section limited at 85 percent of the compressive strength of the concrete. These simplifications led them to propose design expressions of the

shear resistance of the connection in function of required embedment length. Marcakis and Mitchell [3] suggested a different expression of the shear resistance in function of the required embedment length. However, similar results should be obtained using these two approaches, according to Gong and Shahrooz [5].

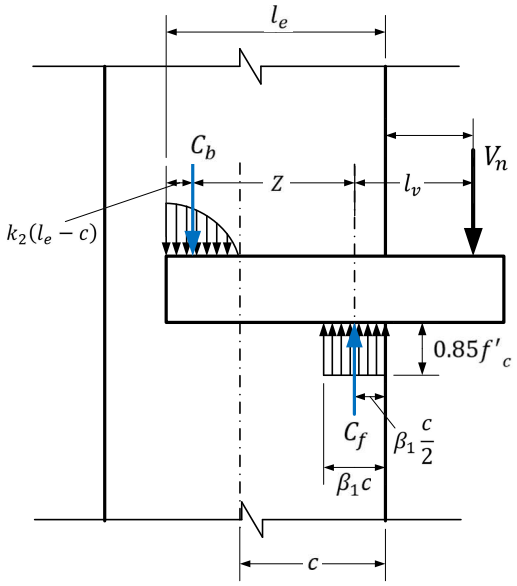


Figure 1: Assumed stress distribution by Mattock and Gaafar [4].

These two design approaches have also been investigated in order to determine required embedded length and strength of steel coupling beams by several studies [5]-[9]. The coupling beams are generally used to connect adjacent reinforced concrete shear walls. They are required to sustain high shear forces and to effectively dissipate energy for high-rise buildings under seismic actions. It was shown by these works that acceptable results were obtained using the aforementioned approaches for the design of the coupling beams. The approach proposed by Mattock and Gaafar [4] was suggested in the design recommendations [10]-[11] with minor modifications for determining the required embedment length of the coupling beams. In the cases of steel brackets connected to reinforced concrete columns, the embedment length usually varies between 0.2 m to 0.5 m, depending on its height. A longer embedment length is rarely used for economic reasons, so not much attention has been paid for this case. However, embedment length of steel coupling beams may be significantly longer, especially when the clear span is long and the shear forces to be transmitted are high [7]. In such a situation, the approach by Mattock and Gaafar [4] is no longer applicable.

Another application of embedded steel profiles is the shearhead reinforcement as the column-to-flat-slab connection [12]-[15]. The connection incorporating shearhead is typically made by a steel insert passing through or welded to the column and embedded in the flat slab. Corley and Hawkins [12] conducted experimental tests on 21 shearhead specimens that confirmed the efficiency of the shearheads in increasing the punching capacity of flat slabs by enlarging the critical shear perimeter. They also proposed a design criterion for the ultimate strength of the shearhead by assuming an idealised shear distribution along the arm of the shear head. Bompa and Elghazouli [15] later investigated the ultimate behaviour of cruciform H-shaped shear-head systems fully embedded into the RC flat slab and welded to the steel column by six large scale tests and suggested analytical design expressions taking into account the effect of embedded length of the shear-heads with or without shear reinforcement.

In a situation of steel balcony-to-concrete slab connections, embedded steel profiles are used to transfer not only shear forces but also large bending moments from the balcony onto the concrete slabs (see Figure 2). Due to the small thickness of the slab, long embedment length might be needed to resist to the shear and bending forces. In this case, the design approaches proposed for steel sections embedded in a reinforced concrete column as brackets might not be applicable, due to the long embedment length and the lower stiffness of the reinforced concrete slab. At the same time, the design criteria for the shearhead might not be valid also in this situation.

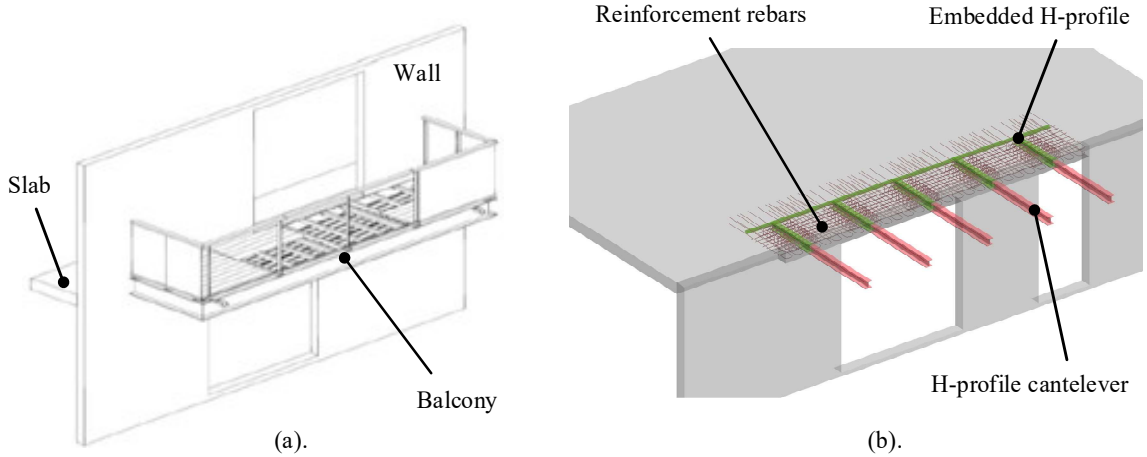


Figure 2: System of demountable balcony: (a). Concept. (b). Components.

This paper investigates the behaviour of long embedded H-profile balcony-to-slab connections by means of a large-scale experimental test and a fully detailed finite element simulation. Detailed results and observations are reported such as moment-bearing capacity, deformation behaviour, the cracking patterns and the distributions of the bending moment along the axis on the embedded steel H-profile as well as the failure mode of the connection system. Based on the results from the experimental test, a 3D finite element model is developed using Abaqus/Explicit [16] and validated. At last, the findings obtained from the validated FE model are used to verify the accuracy of the model of Timoshenko beam on elastic foundation for the design of the long-embedded H-profile balcony-to-slab connection.

## 2. Experimental program

### *2.1 Test setup*

The test setup is conceived to represent a balcony-slab connection (Figure 3a). In order to have a simple test setup and to have a representation of the in-situ moment diagram (Figure 3b), the specimen is conceptualized to be simply supported at the theoretical inflection point of the slab while the load is applied at the free extremity of the cantilever (Figure 3c).

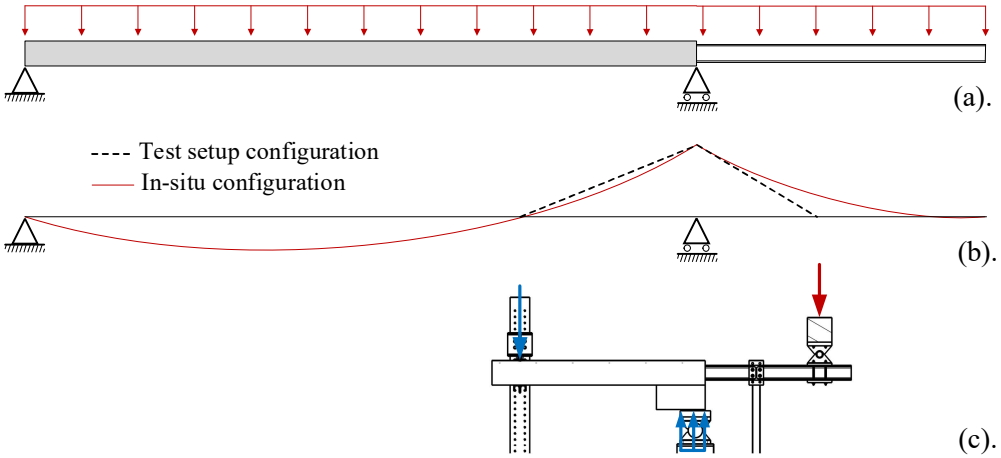


Figure 3: Specimen design: (a). Configuration of real loads on floor-to-balcony connection. (b). bending moment diagrams. (C). Configuration of testing.

Consequently, the test setup is illustrated in Figure 4. It consists of a specimen made of a concrete slab and two embedded steel profiles, a rear supporting frame, two front supporting columns, two lateral bracings, a force jack with a capacity of 1500 kN, and a loading cross-beam to distribute the load from the jack onto the cantilever beams. In this test setup, the specimen was placed on the two front supporting columns with a contact surface of 300mm-by-160mm. A steel plate with a dimension of $160\text{mm} \times 300\text{mm} \times 10\text{mm}$ and an elastomer plate with a thickness of 50 mm were placed between the specimen and the front supporting columns in order to avoid local damage of the concrete (Figure 5e). Two lateral bracings were also installed in order to prevent the lateral buckling of the profiles. Between the lateral bracings and the cantilever steel H-profiles, two layers of PTFE material were installed to reduce friction. The loading was applied vertically by the force jack on the two cantilever profiles through the loading HEB-200 cross-beam, giving a reaction to the concrete slab by the rear support. Different mechanical pins were used between the HEB-200 cross-beam and the two HEB-120 cantilever beams (Figure 5d), on top of the front supporting columns (Figure 5e), and between the HEA-200 cross-beam and the specimen at the rear framed support (Figure 5f). Figure 6 shows the actual photo of the test setup.

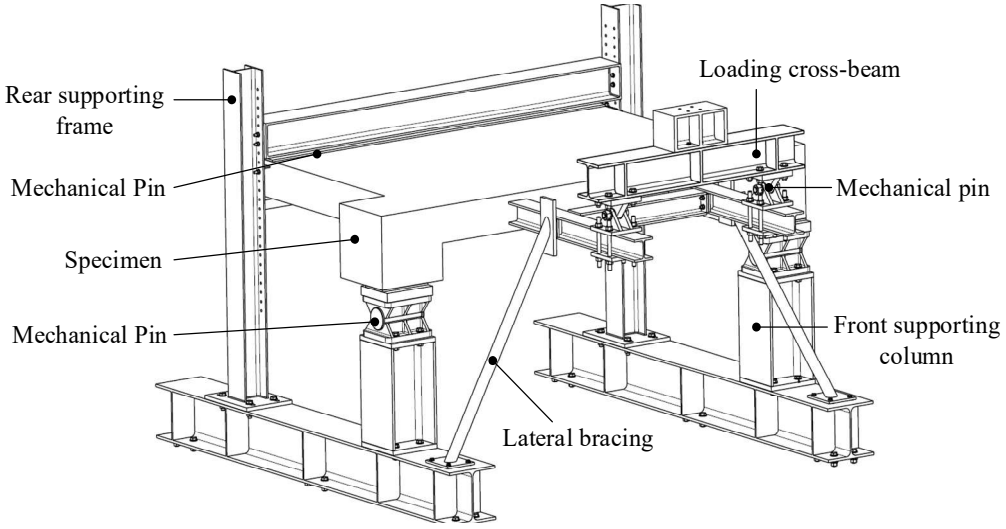


Figure 4: Test setup.

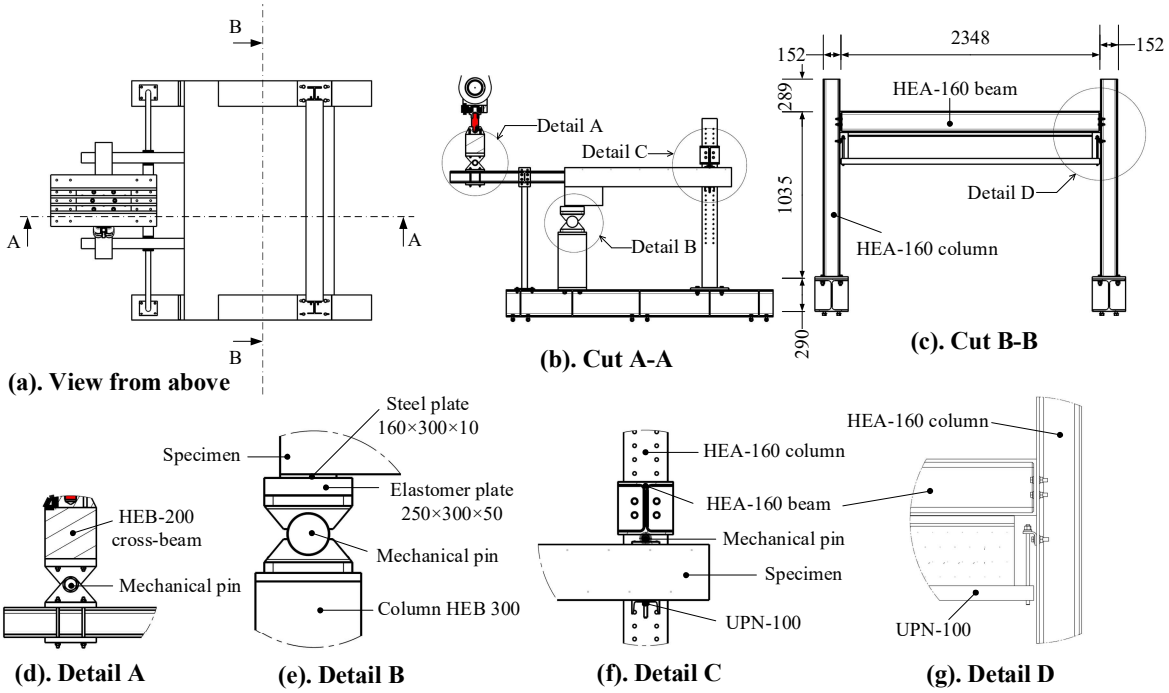


Figure 5: Detail of the support system.

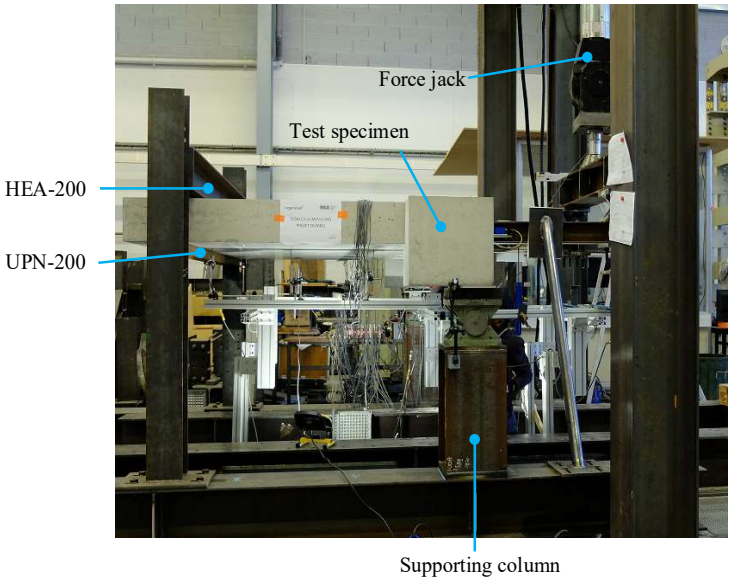


Figure 6: Actual photo of the test setup.

## *2.2 Geometry of the tested specimen*

The specimen was composed of two HEB-120 profiles with a length of 2180 mm, a reinforced concrete slab with a thickness of 200 mm, a steel tube with a section of 50×50×3 mm, an HEB-120 cross-beam and reinforcement rebars (see Figure 7). The reinforcement rebars are not displayed in this figure, but given in Appendix A. The HEB-120 profiles were welded to the steel tube at one extremity to conform with the practice of the industrial partner (see Appendix B), in order to fix the spacing between the profiles and encased with a length of 1 m in the reinforced concrete slab. They were also fixed at the cantilever side with the HEB-120 cross-beam in order to

strengthen the cantilevers against lateral buckling. Concrete drops with a dimension of 400×400×400 mm were added at the contact with the front supports in order to avoid concrete shear failure at the supports.

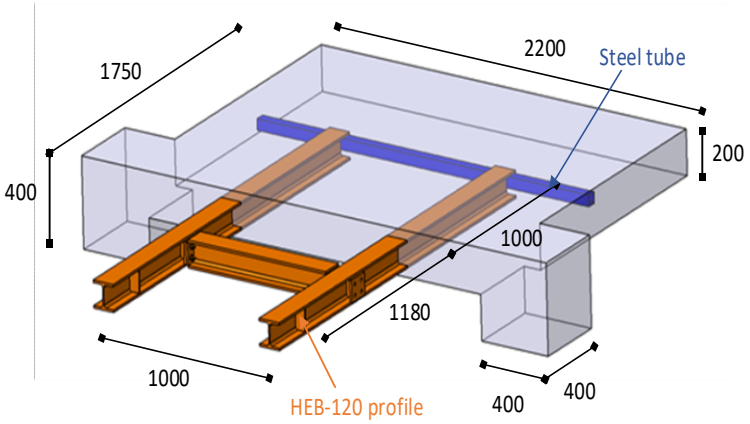


Figure 7: Geometry of the specimen.

## *2.3 Material properties*

The reinforced concrete slab has a strength class of C25/30. In order to obtain the actual characteristics of the materials used on the day of experimental test, compressive concrete tests on three-cylinder samples with a dimension of 11 × 22 cm were carried out following the norm NF EN12390–3 [17]. Regarding the steel elements, the HEB-120 profile and the rebars have a steel grade of S355JR and S500, respectively. 6 and 3 Coupon samples were extracted from the flange and the web of the HEB-120 profile and tested following the norm NF EN ISO 6892-1 [18]. In addition, 3 sample were also made for each diameter of rebars and tested. The results are summarized in the Table 1. $n$ is the number of the samples. $f_{cm}$, $f_{ym}$ and $f_{um}$ are the mean values of the compressive strength of the concrete, of the yield strength and of the ultimate strength of steel elements, respectively. $\sigma$ is the standard deviation. It should be noted that for the tensile tests on rebar specimens, extensometers were not working properly,

**Table 1: Material properties.**

| Elements | | $n$ | $f_{cm}$ [MPa] | $\sigma_{cm}$ [MPa] | $f_{ym}$ [MPa] | $\sigma_{ym}$ [MPa] | $f_{um}$ [MPa] | $\sigma_{um}$ [MPa] |
|---|---|---|---|---|---|---|---|---|
| Concrete | | 3 | 36.9 | 1 | - | - | - | - |
| HEB-120 | Web | 3 | - | - | 386.9 | 16.3 | 509.9 | 6.7 |
| | Flange | 6 | - | - | 395.5 | 7.7 | 515.1 | 7 |
| Rebar | ϕ8 | 3 | - | - | - | - | 621.2 | 14.8 |
| | ϕ10 | 3 | - | - | - | - | 550.1 | 14.3 |
| | ϕ12 | 3 | - | - | - | - | 598.9 | 19.7 |

## 2.4 *Loading procedure and measurement*

The vertical load was applied to the HEB-120 cantilever beams of the specimen through the cross-beam by the force jack with a capacity of 1500 kN. Following the loading procedure provided in Annex B of Eurocode 4 [19], the loading was first applied up to 40 percent of the expected failure load (corresponding to 25 kN), and then cycled 25 times between 5 and 40 percent of the expected failure load. Another cycle between 5 % of the expected failure load and the value estimated for ultimate limit state design (corresponding to 50 kN) was exerted before reloading up to failure. The force was measured by a force sensor DELTECH with a capacity of ± 200 kN.

In order to measure the vertical displacements at various positions of the specimens, 15 LVDT displacement sensors $D_{v1}$ to $D_{v15}$ were installed (see Figure 8). Among them, 11 sensors ($D_{v5}$ to $D_{v15}$) were placed below the concrete slab and 4 sensors ($D_{v1}$ to $D_{v4}$) were placed below the HEB-120 cantilever beams. The sensors $D_{v5}$ and $D_{v9}$ were positioned close to the front supports to measure their settlements. The same was done with sensors $D_{v14}$ and $D_{v15}$ to capture the rigid displacement of the rear support.

In addition, 40 uniaxial strain gauges in total were used to determine the deformation of the embedded HEB-120 profiles along their length at the locations of 30 mm, 80 mm, 180 mm, 280 mm and 380 mm from the front side of the concrete slab (see Figure 9). Four strain gauges (two on top flange and the other two on bottom flange) were installed at each location (cross-section) per steel profile. Figure 10 shows the photos of LVDT sensors during the test and of the strain gauges during the fabrication of the specimen.

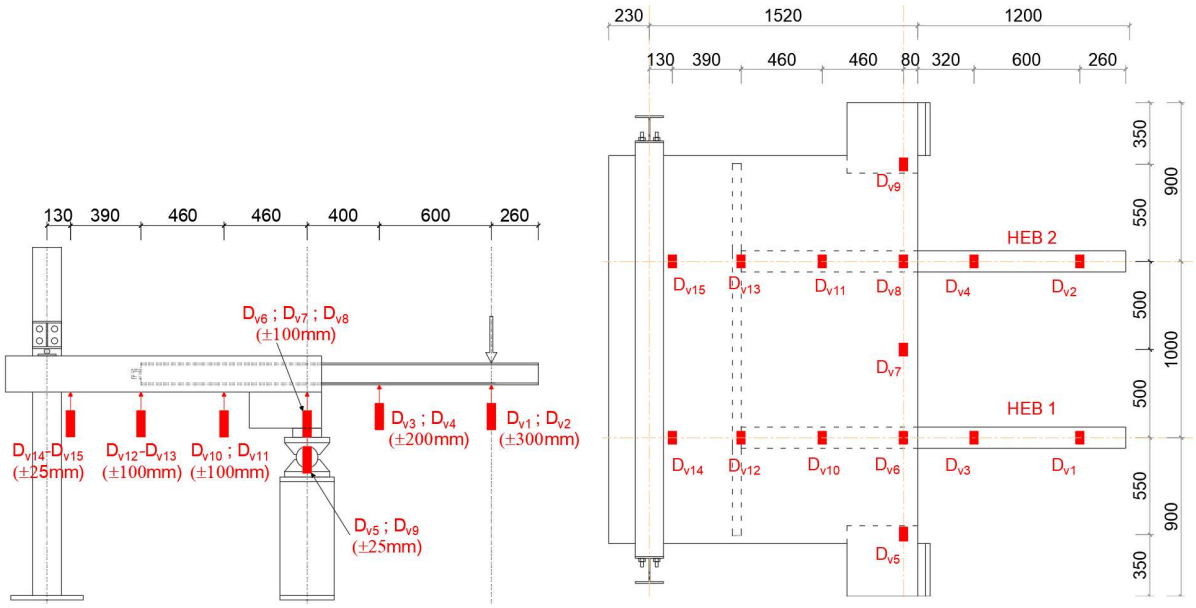


(a). Side view. (b). plan view.

Figure 8: LVDT displacement sensors (dimension in mm).

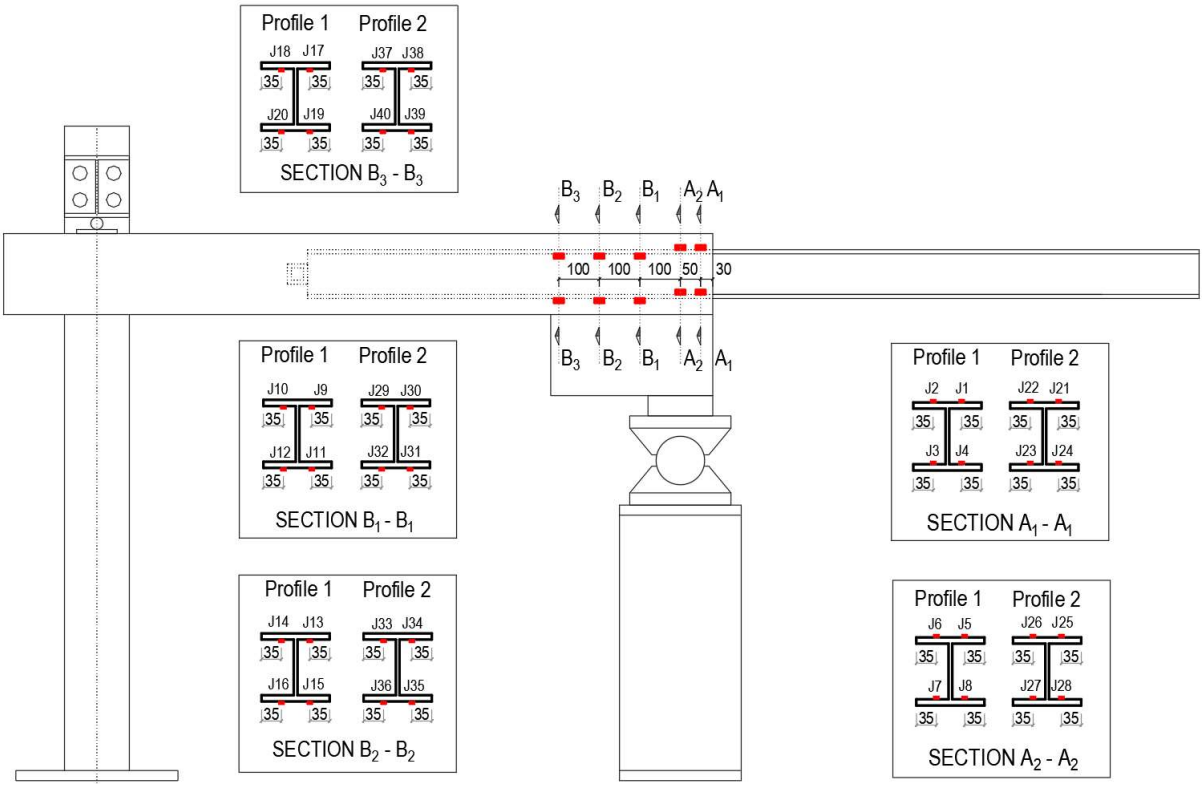


Figure 9: Strain gauges (dimension in mm).

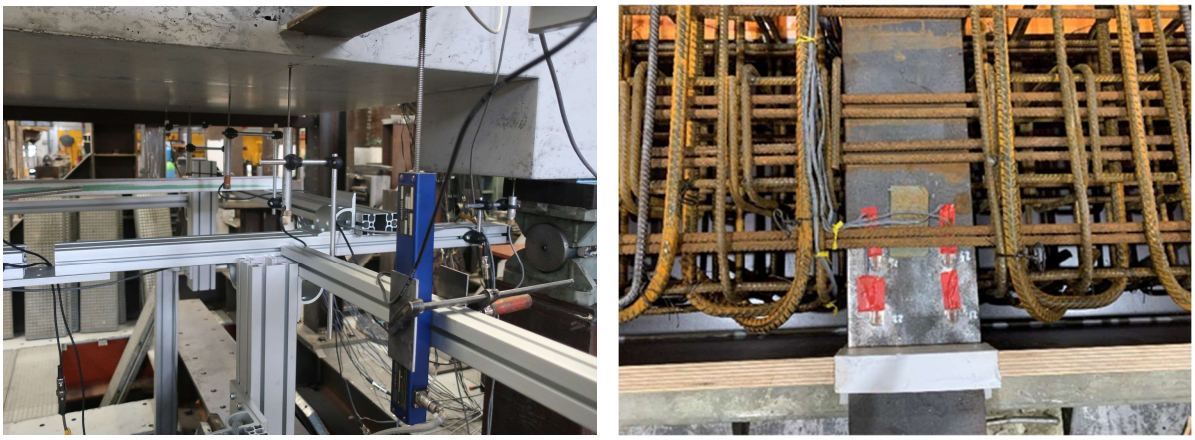

(a). (b).

Figure 10: (a). Photo of the LVDT sensors. (b). Photos of the strain gauges.

## *2.5 Results*

### *2.5.1. Observations and failure mode*

The force-displacement curve illustrated in Figure 11 is used to describe the sequence of the observations during the test. The first cracks of concrete were observed below the embedded steel profiles (see Figure 12) during the cyclic loading between 5 kN and 25 kN. Diagonal cracks that developed from the extremities of both flanges of the profiles were noticed as soon as the loading reached 37.5 kN (see Figure 13a, b and d). These cracks continued

to propagate downward to the bottom surface of the concrete slab (point C and then E). Inclined flexural cracks also appeared at 37.5 kN in the areas between the supports and the steel profiles (see Figure 13a and b). However, these cracks propagated upward to the top surface of the concrete slab (point C, D, E or F), in a reverse direction compared to the diagonal cracks. Additionally, vertical flexural cracks were observed in the middle area between the steel profiles (see Figure 13d).

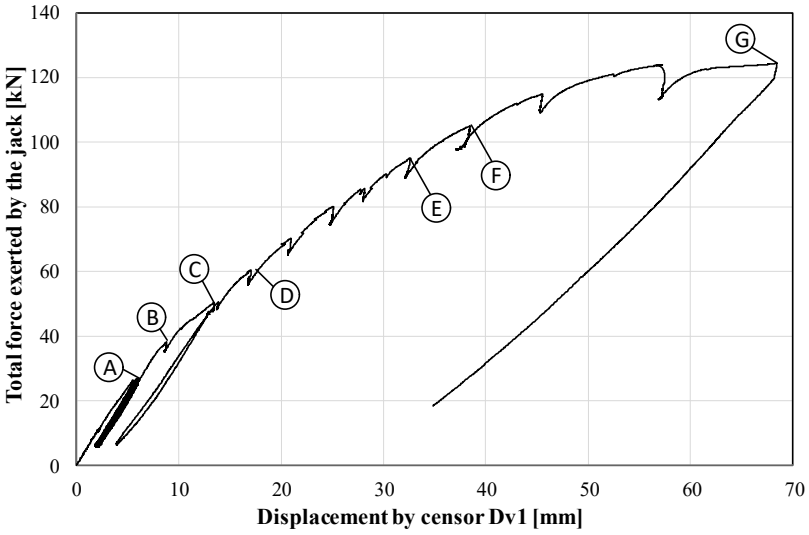


Figure 11: Force-displacement curve of the force jack.

On the bottom surface of the concrete slab, cracks that linked the diagonal cracks were noticed when the loading reached 50 kN (point C in Figure 13e). Besides, inclined cracks were also observed starting from point C (50 kN) on the lateral surfaces of the concrete slab that connected from the flexural cracks on the front surface of the concrete slab. These cracks again propagated upward to the top surface of the concrete. In addition, cracks could be seen on the top surface of the concrete slab, which propagated from the edge inward. The test was stopped at 124 kN once excessive crack openings below the steel profiles and at the corners on the lateral surfaces of the concrete slab were detected (see Figure 13a, f and h).

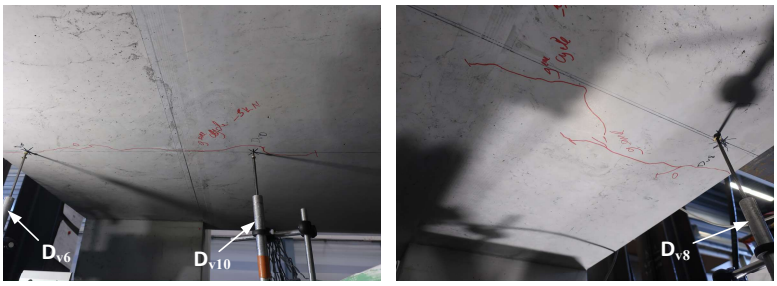


(a). HEB 1. (b). HEB 2.

Figure 12: First cracks during the 25 initial cycled loading.

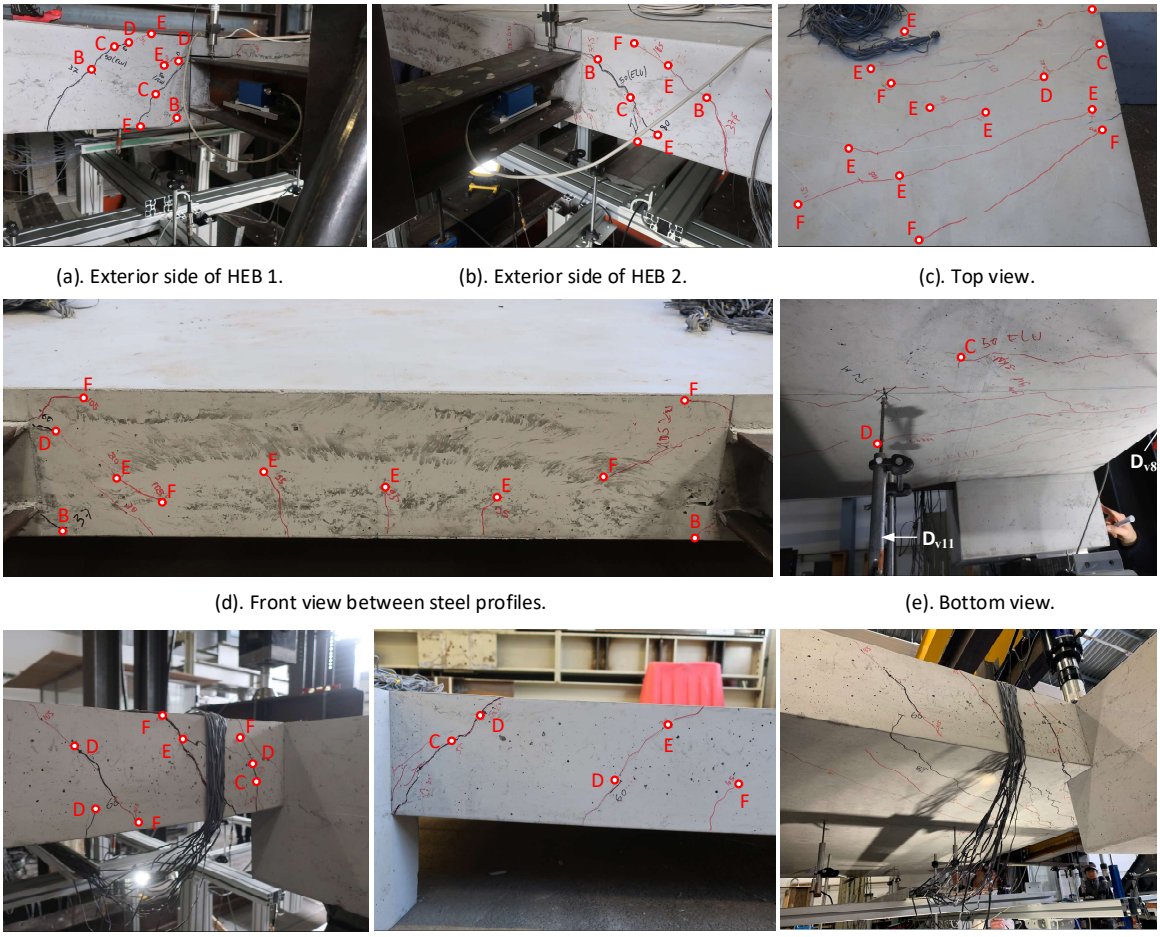


175 Figure 13: Observations during the test.

*2.5.2. Moment-deflection curves*

Figure 15 illustrates the bending moment-deflection curves. The displacements obtained from the sensors include the deflections of the cantilever beams or of the concrete slab as well as the rigid displacements of the whole specimen by the settlement of the polymer plate and the movement of the back support (see Figure 14).

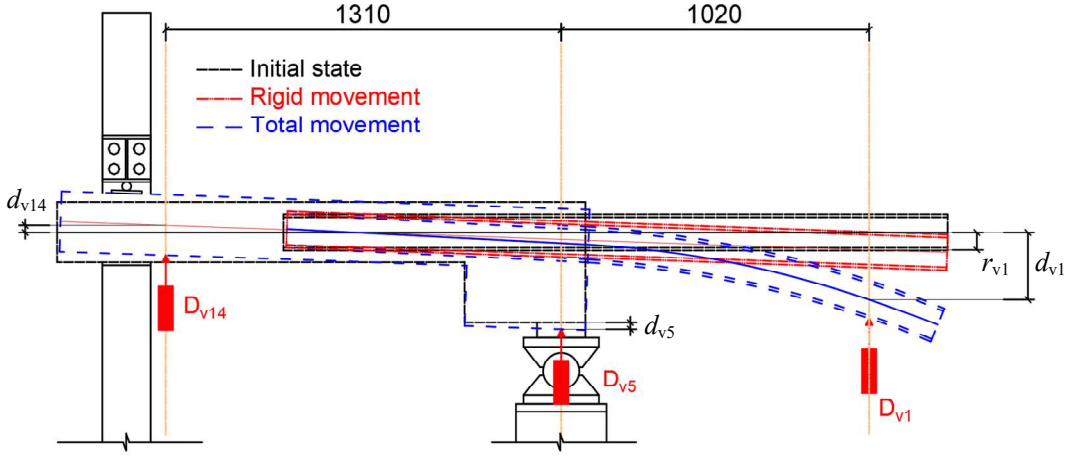


180 Figure 14: Correction of the measured deflections.

The deflections presented in Figure 15 have been corrected by removing the part corresponding to the rigid displacements. The maximum bending moment at the connection obtained per steel cantilever was 63 kN.m and the corresponding deflection by sensor Dv1 was approximately 68 mm.

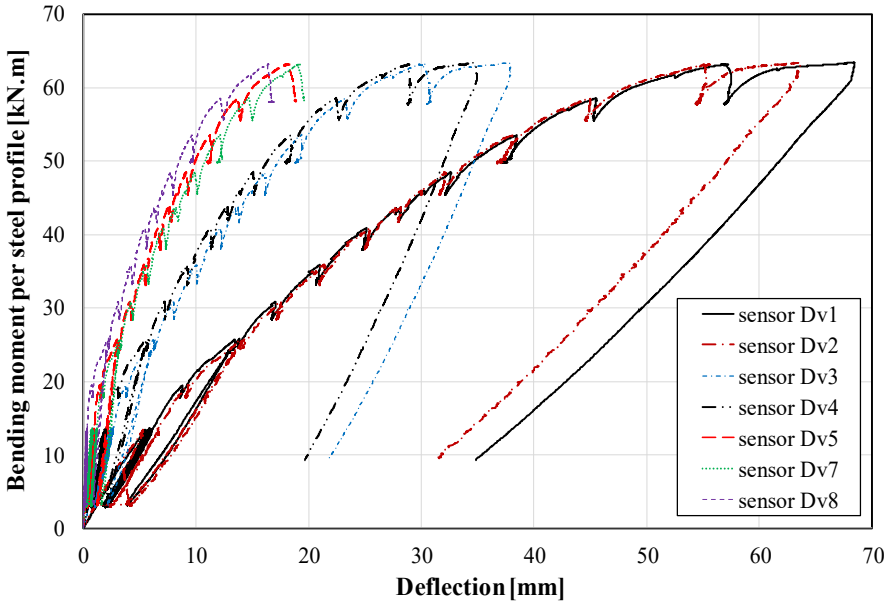


Figure 15: Force-deflection curves.

*2.5.3. Distribution of deformation and bending moment in embedded profiles*

The deformation of the embedded profiles was measured at different locations along the profiles (see Figure 9). The evolutions of the deformation of the steel profiles in function of the applied force per profile are shown in Figure 16 for sections $A_1$-$A_1$ and $A_2$-$A_2$, in Figure 17 for sections $B_1$-$B_1$ and $B_2$-$B_2$, and in Figure 18 for section $B_3$-$B_3$. Only some results of the strain gauges are presented, as some strain gauges were damaged during the fabrication of the specimen. However, it can be concluded from these figures that the embedded steel profiles were yielded on the top flanges at the section $A_1$-$A_1$ when the load reached 100 kN in total force (50 kN, force per profile) and on the bottom flanges when the load arrived at 124 kN in total force. The plastification propagated until the top flanges at the section $A_2$-$A_2$ when the load reached 110 kN in total force.

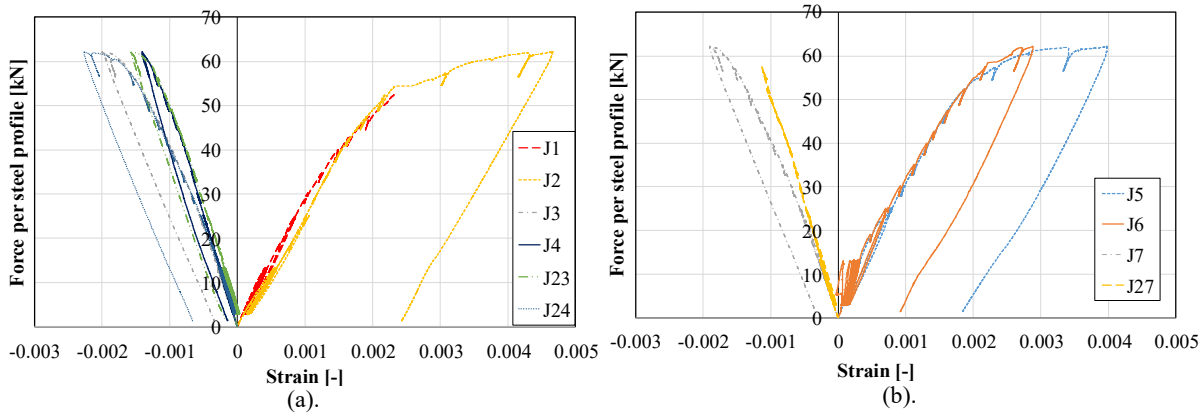


Figure 16: Force-strain curve - (a). Section $A_1$-$A_1$. (b). Section $A_2$-$A_2$.

Based on the results of the strain and of the coupon tests on the specimens of the steel profiles, the distribution of the bending moment on the embedded steel profile HEB 2 is determined at different load levels and presented in Figure 19. It should be noted that the bending moment acting on each cross-section of the embedded steel profile is computed based on the assumption that the strain varies linearly on the cross-section for both elastic and elastic-plastic behaviours (see Figure 20). Regarding the elastic-plastic behaviour, the stress is considered to be limited at $f_y$, as the results of coupon tests have shown that the plastic flow was between 0.002 and 0.018 before hardening of the material. The results obtained from strain gauges gave the maximum deformation of 0.0047, meaning that the stress remained limited at $f_y$.

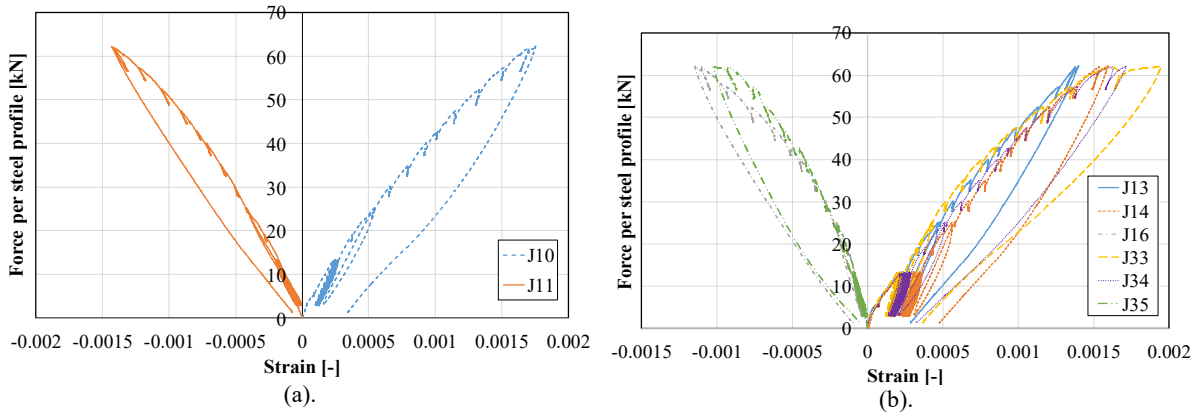


(a). (b).

Figure 17: Force-strain curve - (a). Section $B_1$-$B_1$. (b). Section $B_2$-$B_2$.

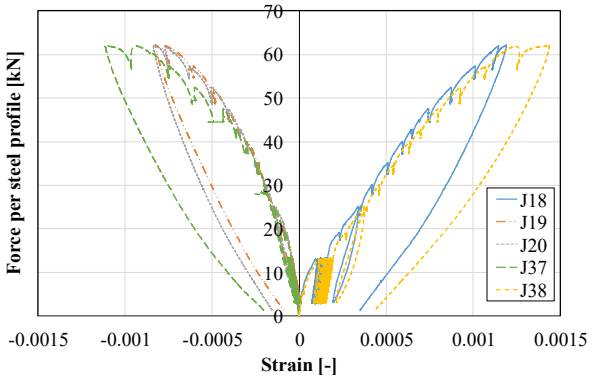


Figure 18: Force-strain curve - Section $B_3$-$B_3$.

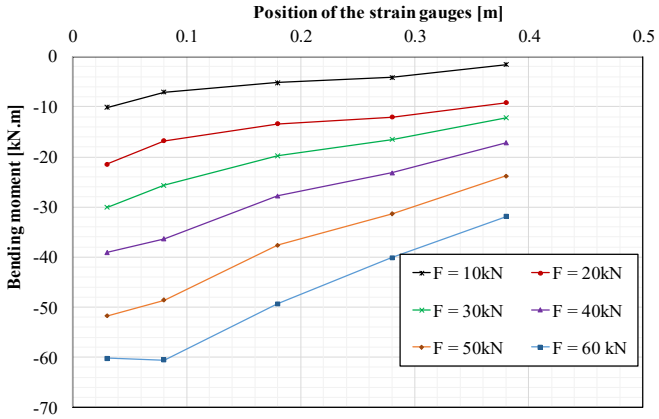


Figure 19: Evolution of the bending moment along the embedded profile HEB 2 at different load levels (force per profile).

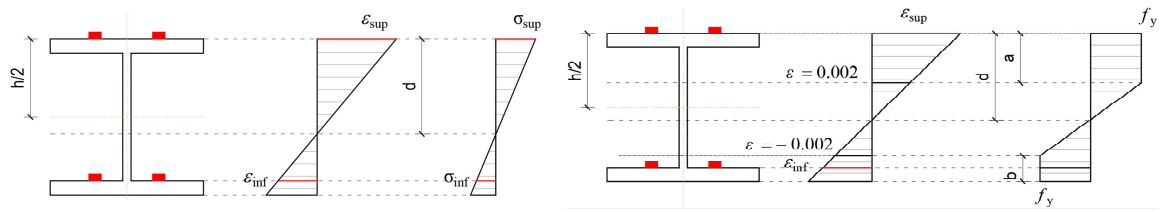


(a). Elastic range (b). Elastic-plastic range

Figure 20: Distribution of stress and strain on the cross-section (Section $A_1$-$A_1$).

*2.5.4. Comparison of maximum force and bending moment*

As being already discussed in the introduction, the design shear capacity of embedded steel brackets inside RC columns can be determined by the expressions proposed by Mattock and Gaafar [4]. In this section, the ultimate shear and bending capacities of the embedded H-profile balcony-to-slab connection are estimated using these expressions, as reported below:

$$V_n = 0.85 f_c \beta_1 b l_e \left( \frac{0.58 - 0.22\beta_1}{0.88 + \frac{a}{l_e}} \right) \quad (1)$$

$$M_{max} = V_n \left( a + \frac{V_n}{1.7 f_c b} \right) \quad (2)$$

where $f_c$ is the mean concrete compressive strength, $b$ is the width of the embedded H-profile, $l_e$ is the embedded length of steel profile in concrete, $a$ is the span of the shear force (taken equal to 0.92 m), and $\beta_1$ is taken equal to 0.85. Using Eqs. (1) and (2) with $f_c = 37$ MPa and $b = 120$ mm, the ultimate shear and bending capacities are determined and reported in Table 2. Using the expressions by Mattock and Gaafar [4] overestimates the ultimate shear and bending capacities by 1000 percent compared to the experimental results. Clearly, this estimation is wrong as expected. This is because the expressions by Mattock and Gaafar [4] were derived based on the assumptions that the concrete below and above the embedded profile had infinite depth and that the embedded profile is rigid. Such assumptions are not valid for the case of the present embedded H-profile balcony-to-slab connection, as its behaviour is impacted by the small thickness of the concrete slab and the plastification of the embedded profile. In addition, this approach does not allow to determine the distribution of shear and bending forces in the concrete slab for the design of the reinforcement rebars.

**Table 2: Ultimate shear and bending capacities using expressions by Mattock and Gaafar [4].**

| | Ultimate shear $V_n$ [kN] | Max. moment $M_{max}$ [kN.m] |
|---|---|---|
| Experimental results | 62 | 63 |
| Estimation [4] | 700.4 | 709.3 |

## 3. Finite element simulation

In order to gain more insights on the load transfer mechanism at the steel-concrete connection, a full 3D FE model of the experimental test has been developed in Abaqus/Explicit [16]. Only half of the specimen was simulated with respect to symmetric conditions of loading, boundary conditions and geometry (see Figure 21a). In addition, all the components in the specimens were included in the model (see Figure 21b). The description of the model is provided in the following sections.

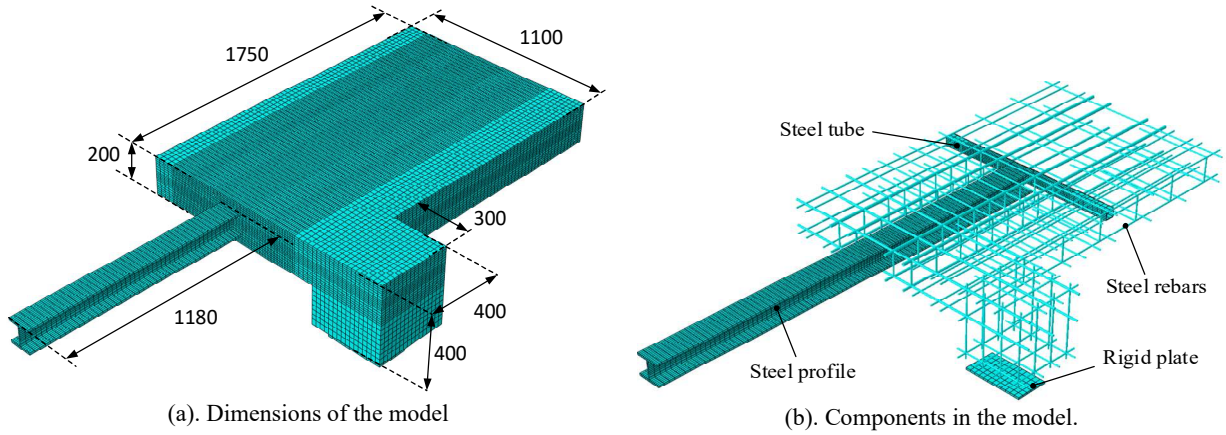


(a). Dimensions of the model

(b). Components in the model.

Figure 21: FE model of the experimental test.

### *3.1 Element type and mesh*

Different element types were used for each component. The concrete slab, the steel profile, the steel tube and the rigid plate were meshed using an 8-node brick solid element (C3D8R) with one integration point and three degrees of freedom at each node. The rebars, on the other hand, were meshed using a 2-node beam element (B31). The meshing of the concrete part around of the embedded steel profile was refined with a size of $10 \times 10 \times 25$ mm (see Figure 21a). The rest of the concrete has an element size of $10 \times 25 \times 25$ mm or $25 \times 25 \times 25$ mm. The overall mesh size of the steel profiles, the steel tube, the rigid plate and the steel rebars are $10 \times 11 \times 27$ mm, $22 \times 27.5 \times 3$ mm, $25 \times 25 \times 10$ mm, and 25 mm, respectively (see Figure 21b). A refined mesh as small as $10 \times 11 \times 15$ mm was also used at the embedded part of the steel profiles.

### *3.2 Constraints and contact interactions*

Different constraints available in Abaqus/Explicit were applied to describe the interactions between the components. An explicit general contact interaction was used to model the contact behaviour of the concrete slab with the steel profiles, the steel tube and the rigid plate. The contact properties were defined by hard contact and friction penalty formulations for the normal and tangential behaviour, respectively. For the frictional contact, a friction coefficient of 0.3 was used. The surfaces in contact between the embedded profile and the steel tube were tied together, being consistent with the actual test specimen where they were tied by welding. In addition, embedded constraint was applied to the rebars placed inside the concrete slab.

### 3.3 *Boundary conditions and loading*

As only half of the specimen was simulated, a proper symmetric boundary condition was applied to the median plane of the model, constraining the displacement in X-direction as illustrated in Figure 22b. Then, the boundary conditions were applied to represent the actual situations in the test setup (see Figure 22a). Firstly, the mechanical pin of the front supporting columns was represented by the reference point 1 that governs the rigid movement of the rigid plate (see detail 1 in Figure 22b). At this reference point, all the degrees of freedom were blocked, except the displacement in X-direction ($U_x$) and the rotation in X-direction ($R_x$). It should be noted that the rigid plate had the same dimension as the steel plate did (160 × 300 × 10 mm). Secondly, the displacement in X-direction ($U_x$) on the lateral surfaces of the top and bottom flanges as well as the web of the H-profile cantilever was constrained at the location of the lateral bracings. At the back frame support, the displacements in X-direction ($U_x$) and in Y-direction ($U_y$) were blocked at the lateral and top surfaces, respectively. At last, to apply the load in accordance with the actual loading configuration in the experimental test, the reference point 2 was created at the location of the mechanical pin (see detail 2 in Figure 22b), governing a rigid displacement of a 200-mm segment of the steel cantilever. The loading was then applied to the reference point through an imposed displacement in Y-direction. All the other remaining degrees of freedom of the reference point were fixed.

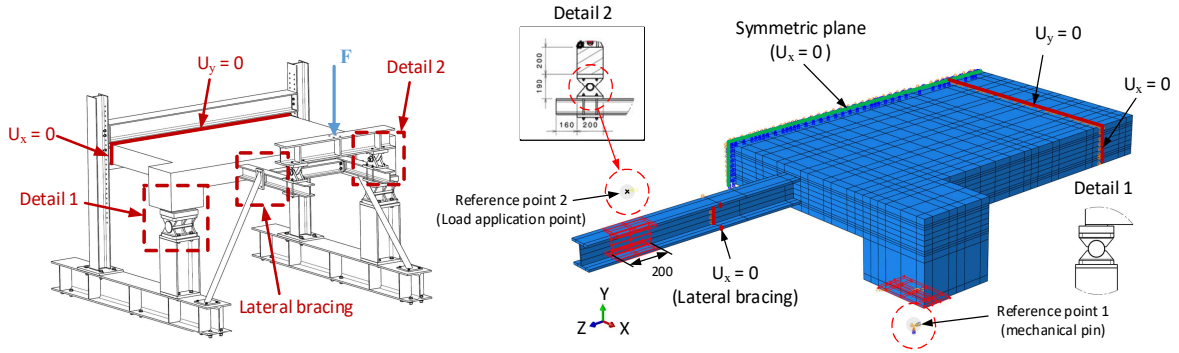


(a). Experimental test setup. (b). FE Model.

Figure 22: Boundary and loading conditions.

### 3.4 *Material models*

The concrete behaviour in this simulation was modelled by the Concrete Damage Plasticity model available in Abaqus/Explicit. The constitutive relations described in [20] was adopted. The uni-axial compressive stress – strain curve and the tensile stress – crack width curve were defined for the nonlinear behaviour of the concrete, as illustrated in Figure 23. The values of the Young's modulus, the compressive resistance and the tensile resistance are 31000 MPa, 37 MPa and 2.6 MPa, respectively. The parameters used in the model are the following: the dilation angle $\psi = 40°$, eccentricity $\epsilon = 0.1$, the stress ratio $\sigma_{b0}/\sigma_{c0} = 1.16$ and the shape factor $K_c = 0.667$.

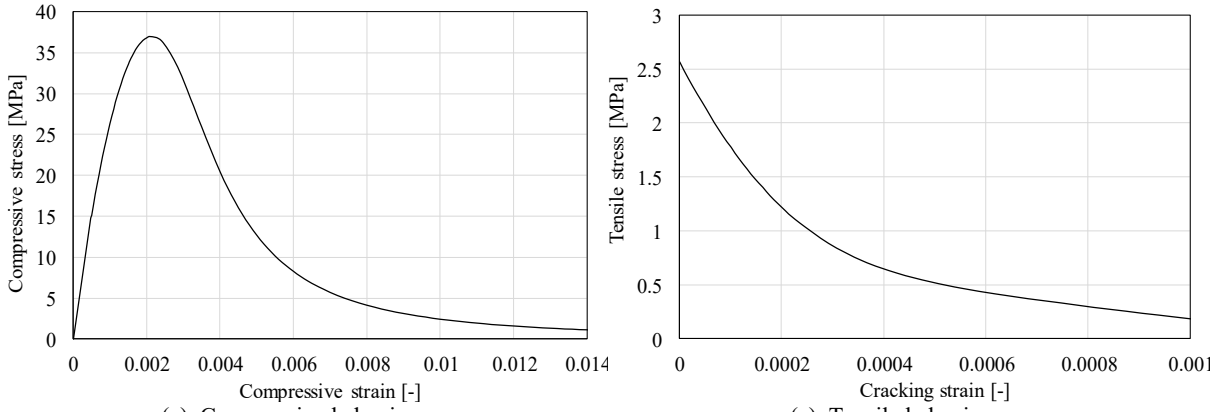


(a). Compressive behaviour. (a). Tensile behaviour.

Figure 23: Constitutive concrete model.

Regarding the steel profile, the actual stress-strain curve obtained from the coupon test was used, as illustrated in Figure 24. On the other hand, the stress-strain relation for the rebars was modelled by a bi-linear curve, as represented by Figure 24b. It should be noted that these curves have already been converted to true stresses – true strains curves for the input in Abaqus/Explicit.

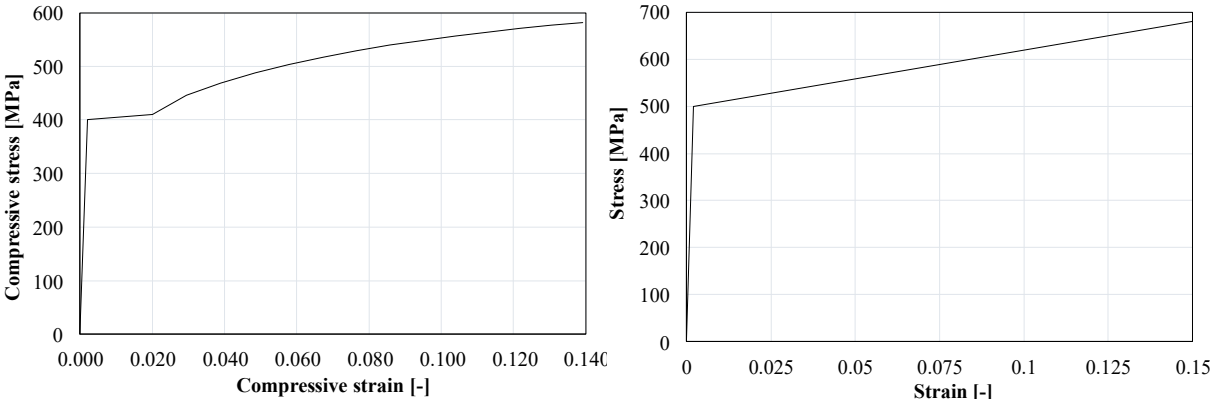


(a). Steel profile. (b). Rebars.

Figure 24: Constitutive steel models.

## *3.5 Validation of the FE model*

In order to validate the FE model, the results such as the force-deflection curves, the failure mode, the cracking pattern and the deformation in the embedded profiles as well as the distribution of the bending moment are compared with the ones obtained from the experimental test.

Figure 25 shows the comparison of the force-deflection curves obtained from the experimental test with the ones obtained from the FE model. A rather good agreement is achieved. The difference of the maximum forces is approximately 3 percent. It has also been observed that the FE model is able to accurately predict the deflections of both the cantilever beams ($D_{v1}$ and $D_{v3}$) and the concrete slab ($D_{v6}$ and $D_{v7}$).

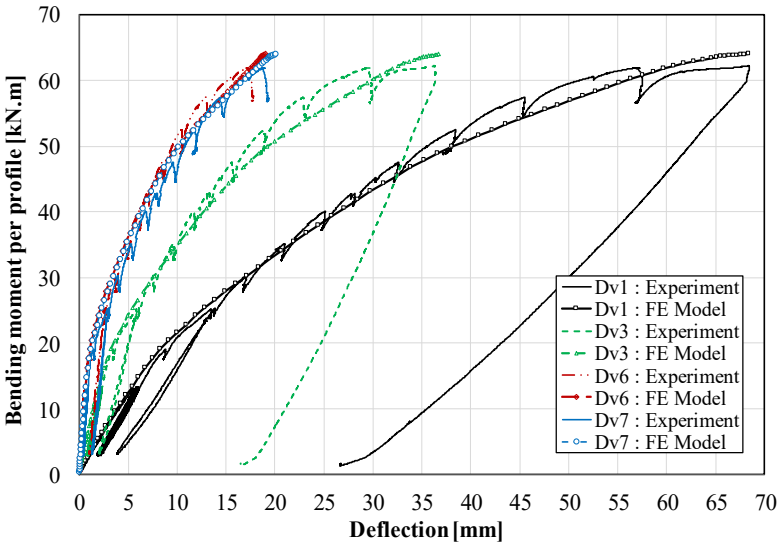


Figure 25: Comparison of force-deflection curves.

The crack observations made in the experimental test were also reproduced in the FE model at different load levels. The tensile damage parameter of the FE model is illustrated Figure 26 in comparison with the cracking patterns in the experimental test. The crack below the profile appeared and the inclined cracks were initiated from the top and bottom flanges of the H-profile in the FE model, in agreement with the observations in the experimental test. At the load level of 35 kN, similar to the observations made in the experimental test, the inclined cracks propagated downward to the bottom surface of the concrete slab with an inclination angle of approximately 54 degrees with respect to the vertical in the FE model. Several more parallel cracks on the bottom surface of the slab also appeared. The FE model exhibited lateral and corner cracks at the maximum load, consistent with the experimental results.

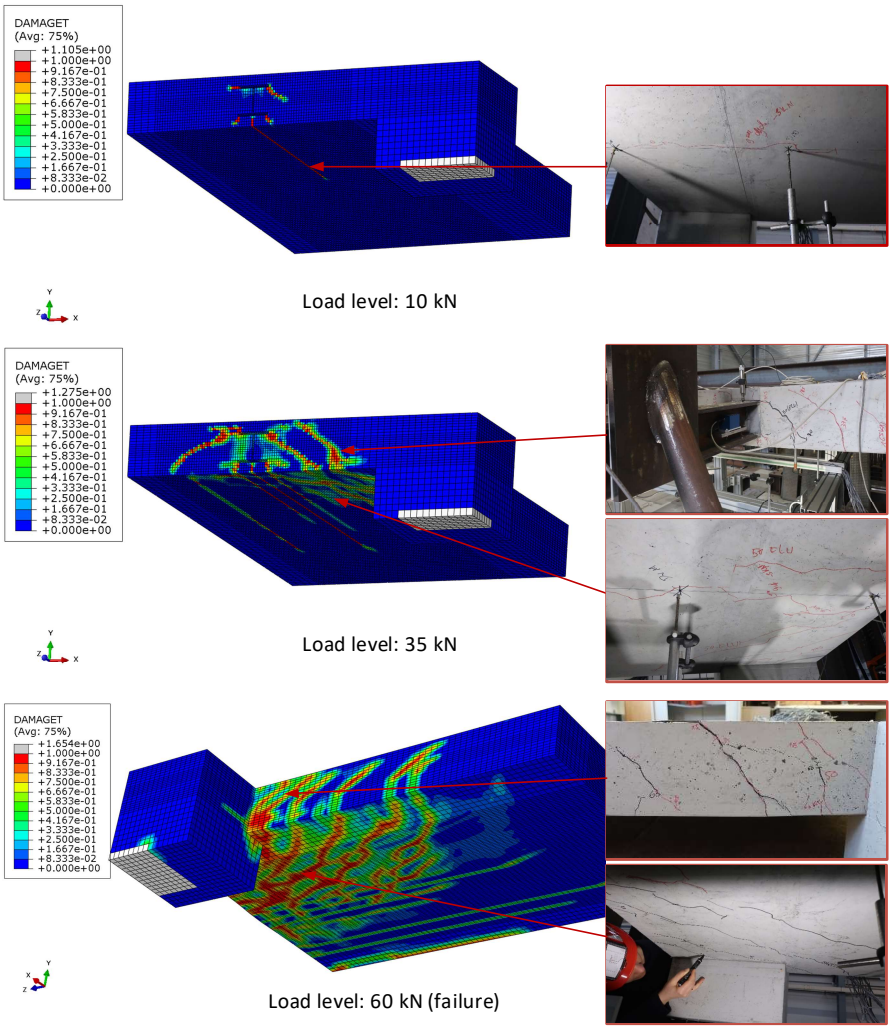


Figure 26: Comparison of the cracking patterns.

305 Figure 27 to Figure 29 provide the comparison of the evolutions of strains in function of the force per profile between the results obtained from the FE model and from the experimental test. It can be seen from these figures that a rather good agreement between the two results was obtained. A better fit of the strains can be observed at the cross-sections $A_2$-$A_2$ and $B_1$-$B_1$.

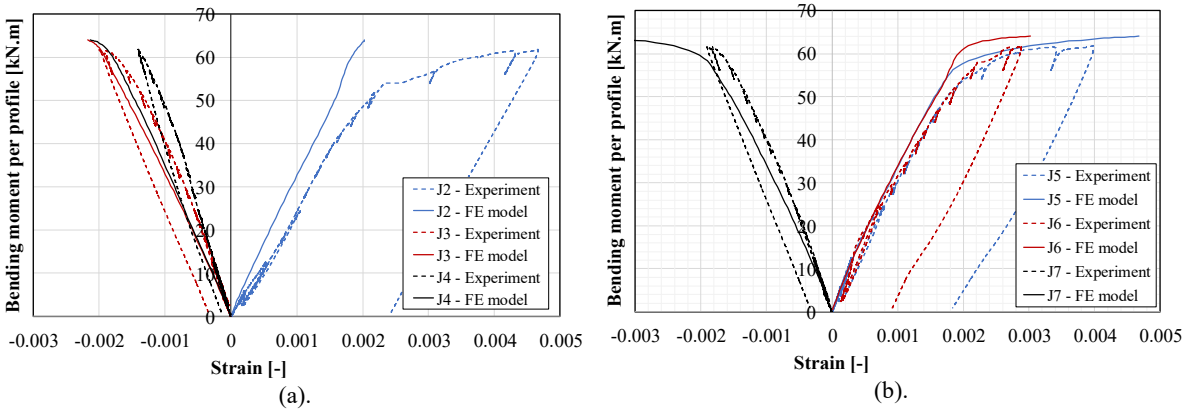


Figure 27: Comparison of force-strain curves - (a). Section $A_1$-$A_1$. (b). Section $A_2$-$A_2$.

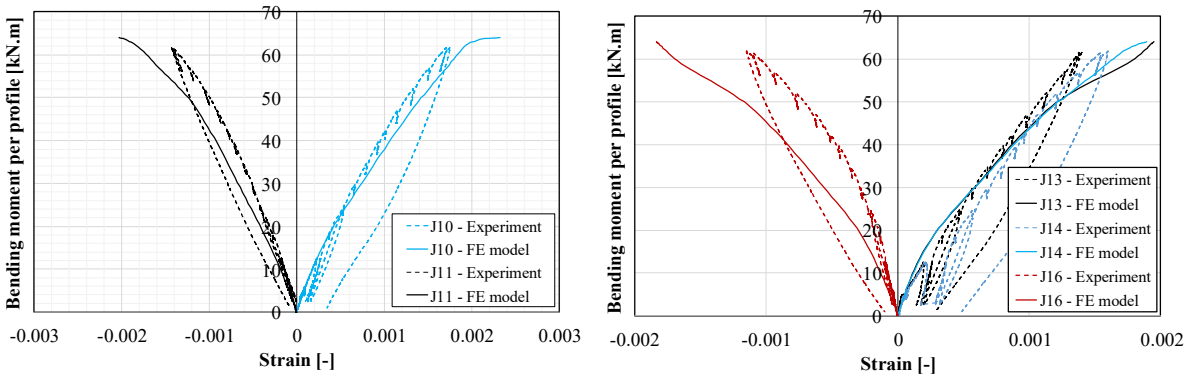


(a). (b).

Figure 28: Comparison of force-strain curves - (a). Section $B_1$-$B_1$. (b). Section $B_2$-$B_2$.

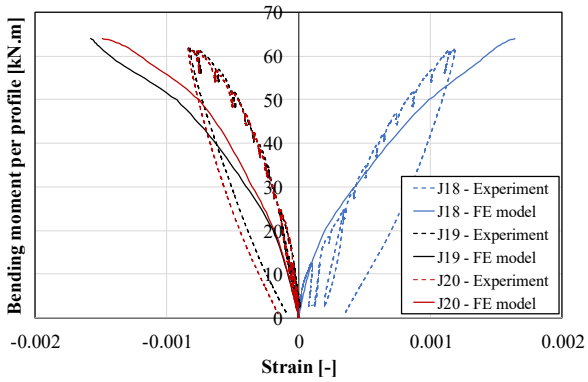


Figure 29: Comparison of force-strain curves - Section $B_3$-$B_3$.

Furthermore, the comparison of the bending moment distribution along the axis of the embedded profile at different load level (load per profile) is given in Figure 30. A strong correlation between the two results was observed until a load level of 40 kN. It can be also noticed that the bending moment is maximum at the distance of 80 mm from the edge of the concrete slab (0 m), corresponding to half width of the support. From this point forward, it has a steady decrease until zero at the extremity of the embedded profile (1 m).

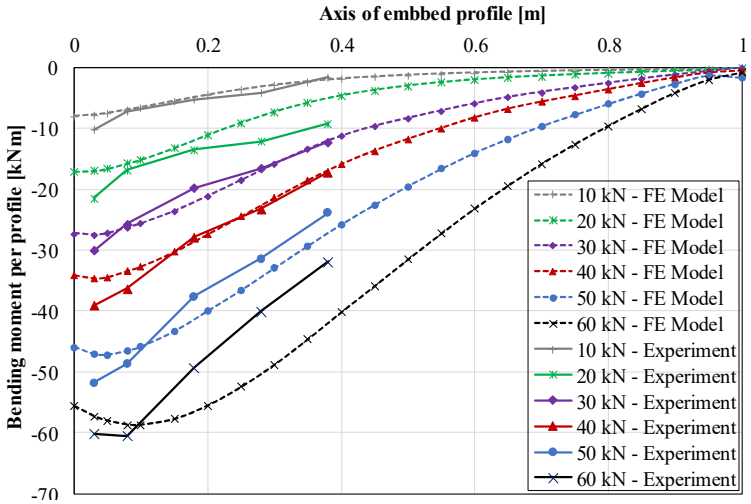


Figure 30: Comparison of the distribution of bending moment at different load level (load per profile).

In overall, the results obtained from the FE model are in good agreement with the experimental observations. The FE model is able to reproduce the global behaviours such as the deflections of the cantilever beam and the concrete slab, the distribution of bending moment along the axis of embedded profile, and the deformations of the embedded steel profile as well as the degradation of materials (cracking and crushing of the concrete) observed in the experimental tests. It can then be concluded that the FE model has been well validated against the experimental tests.

### *3.6 Distribution of shear forces and bending moments*

The FE model also allows to deduce useful information that was not available in the experimental test. Using the model, the shear forces and bending moments acting on the embedded steel profile, the concrete slab and the composite section were determined at different load levels per profile and illustrated in Figure 31 and Figure 32, respectively.

It can be noted from Figure 31 that, starting from the concrete edge, the shear forces in the embedded H-profiles increase from a negative to a positive value with a maximum reached at the abscise of around 0.15 m at the load level of 10 kN and 0.4 m at the load level of 60 kN. This change in the position of the maximum is linked to the degradation of supporting capacity by the surrounding concrete around the embedded H-profiles due to the damage. On the other hand, the shear forces applied to the concrete section are zero at the beginning of the H-profile embedment and increase in a negative value until a peak at around 0.1 m from the concrete edge at a load level of 10 kN and 0.35 m from the concrete edge at a load level of 60 kN. It can be also confirmed from the figure that, for all the load levels, the shear forces applied on the composite section, noted by $V_T$, are the sum of the forces applied to the H-profile (noted by $V_s$) and to the concrete sections (noted by $V_c$), as defined below:

$$V_T = V_s + V_c \tag{3}$$

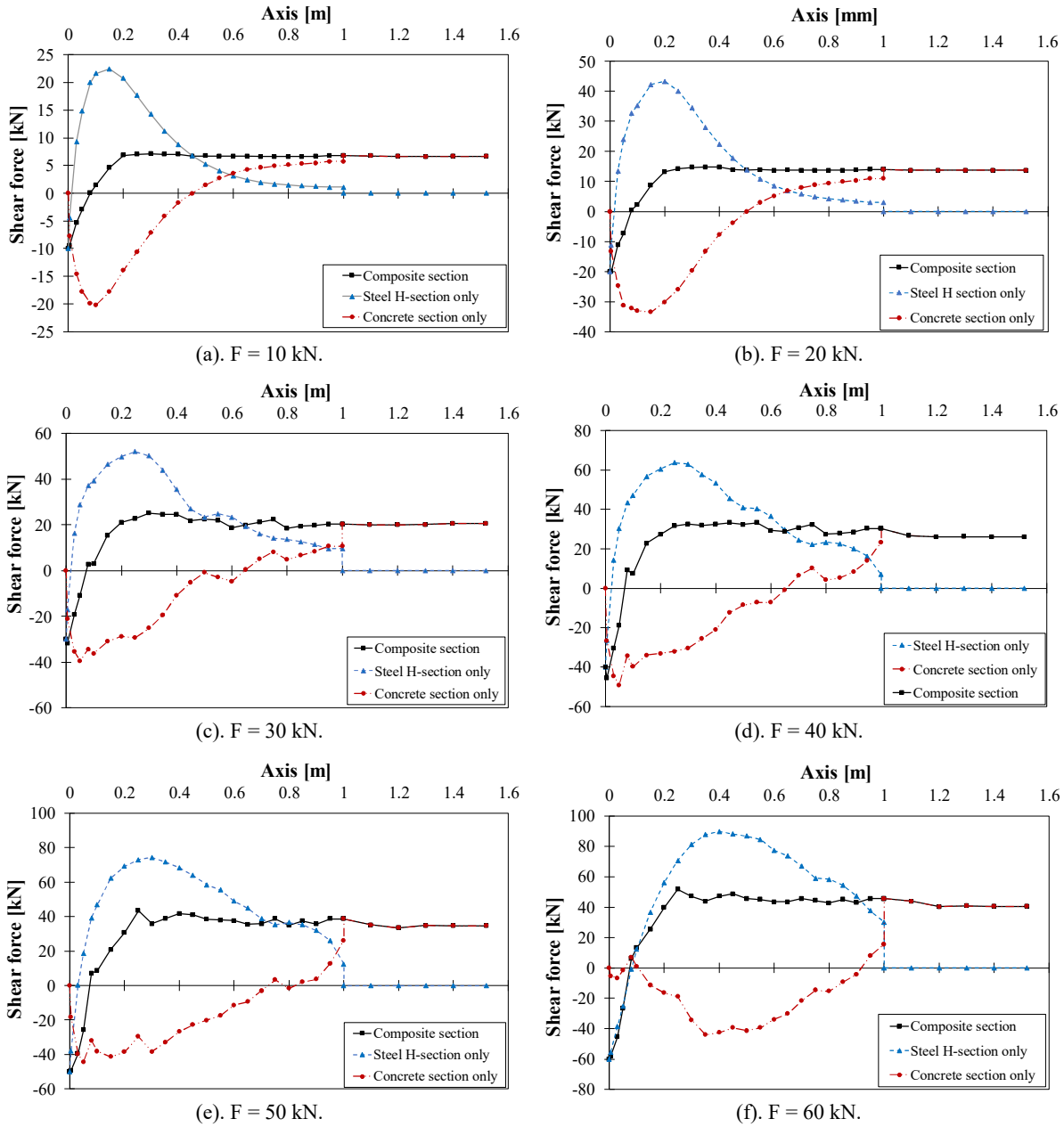


Figure 31: Distribution of shear force on steel, concrete and composite sections at different load levels (per profile).

From Figure 32, it can be observed that the applied bending moments drop from an initial negative value at the beginning of the embedment of the profile (axis = 0m) to a zero value at the end of the embedment (axis = 1m). The bending moments applied to the concrete section increase from a zero value to a peak in negative value at the axis of 0.45 m at the load level of 10 kN. Starting from a load level of 30 kN, a plateau of bending moments between the axis of 0.45 m to 1 m is observed. The figure also suggests that, for all the load levels, the bending moments applied to the composite section, noted by $M_T$, is the sum of the bending moments applied to the H-profile (noted by $M_s$) and to the concrete sections (noted by $M_c$), as defined below:

$$M_T = M_s + M_c \quad (4)$$

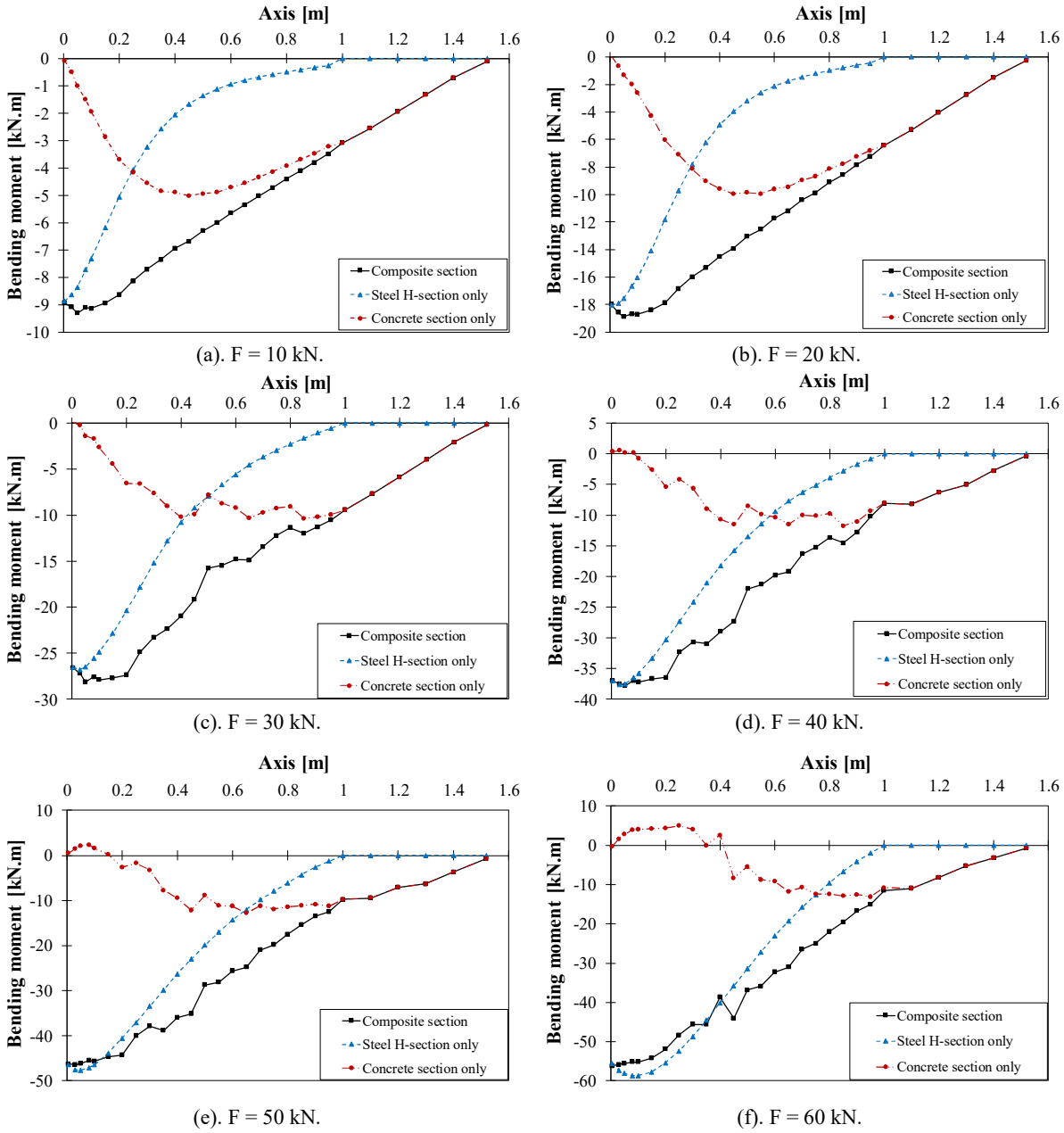


(a). F = 10 kN. (b). F = 20 kN.

(c). F = 30 kN. (d). F = 40 kN.

(e). F = 50 kN. (f). F = 60 kN.

Figure 32: Distribution of bending moment on steel, concrete and composite sections at different load levels (per profile).

It is worth noting that the solution from the finite element model is only an approximation of the real problem, especially for the behaviour of concrete with damage, as set in evidence by the fluctuation of the curves in Figure 31 and Figure 32.

## 4. Analytical methods for the distribution of bending and shear forces

It has been shown above in section 2.5.4 that the approach by Mattock and Gaafar [4] is not satisfying for the design of the embedded H-profile balcony-to-slab connection, i.e. both the embedded H-profile and the reinforced concrete around it. Consequently, there is a need to develop an analytical approach to determine the internal forces in the steel-concrete connection.

In structural analysis, for determining the distribution of the forces in each member, a conventional method based on elastic theory is commonly adopted. In this section, a linear elastic method based on the model of beam on elastic foundation is then proposed in order to determine the shear and bending forces in the embedded H-profile and the reinforced concrete. To the knowledge of the authors, this approach is the first tentative design basis for such a system. In this approach, it is assumed that the global behaviour of the concrete slab supporting the balcony has a little influence on the distribution of the contact forces between the concrete and the steel profile, and therefore only the local contact stiffness must be modelled. This strong hypothesis is made to obtain a simple model, convenient for practitioners, even if it might limit the accuracy.

## *4.1 Composite section*

For the design of the embedded H-profiles and the concrete slab, it is necessary to determine the applied shear forces and bending moments on their cross-sections along the axes in function of the applied forced on the H-profile cantilever beams. This section is devoted to using analytical approaches to estimate these parameters.

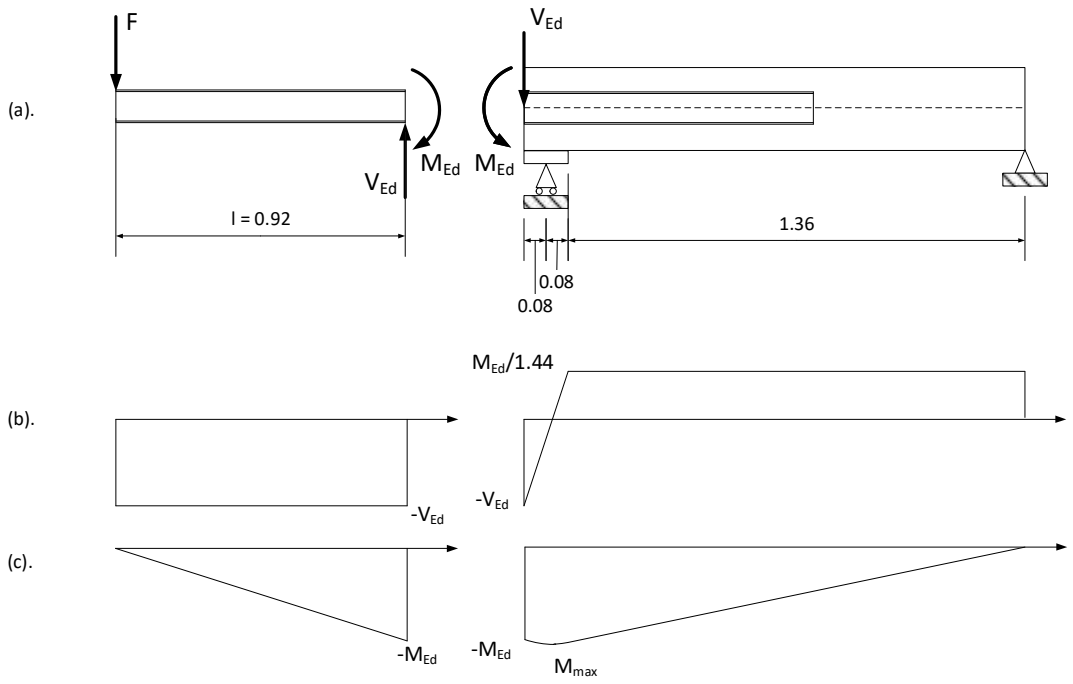


Figure 33: Representing system of the test setup: (a). beams on simply supports. (b). shear force diagram. (c). Bending moment diagram.

Assuming that the test setup and the FE model described in Section 2 and Section 2.5.4, respectively, can be represented by a beam on simply supports as illustrated in Figure 33, the bending moments and shear forces applied on the composite section can be determined analytically based on beam theories. The applied shear and bending forces at the edge of the concrete (embedded point) are the following :

$$M_{Ed} = 0.92F \quad (5)$$

$$V_{Ed} = F \quad (6)$$

Figure 34 illustrates the bending moment and the shear force on the composite section obtained from the beam theory in comparison to those obtained from the FE model. It is evidently demonstrated in this figure that the

results are consistent with the ones obtained from the FE model for the computation of the bending moments and shear forces acting on the composite section, for a load level lower than 20 kN. For a larger load level, the concrete experiences severe damages, and the FE results show irregularities with fluctuation of the curves coming from the approximation by explicit finite element solution.

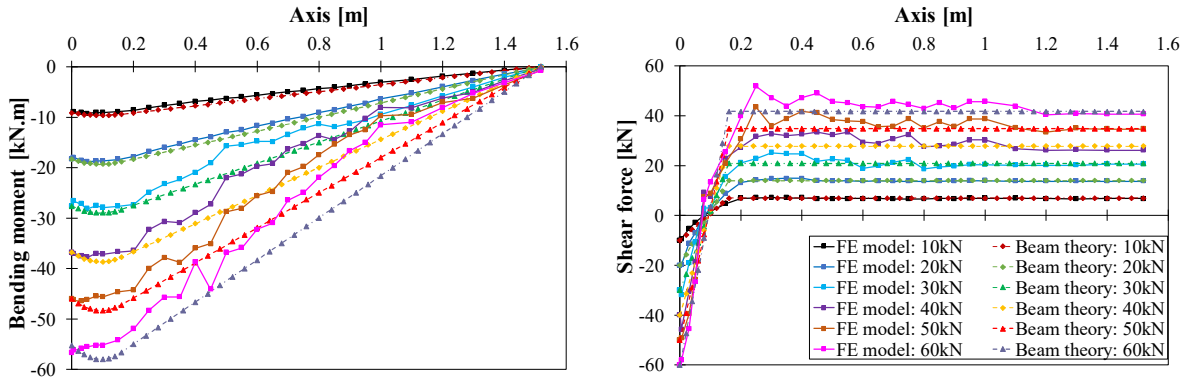


(a). Bending moment. (b). Shear force.

Figure 34: Comparison of bending moments and shear forces on composite sections at different load levels (per profile).

## *4.2 Steel and concrete sections*

This section is devoted to determining the distribution of shear and bending forces on the embedded profiles and the concrete sections. For the forces applied to the embedded steel profile alone, a model of beam on elastic foundation (BEF) might be considered. Once these forces are known for the steel profiles, the ones on the concrete section can be determined using Eqs. (3) and (4). The description of the BEF model is given in the following sections.

### 4.2.1 *Beam model on elastic foundation*

For the forces applied to the embedded steel profile alone, a beam model on elastic foundation (BEF) might be considered. This model type has been proposed in several occasions for embedded structural elements such as dowel-type rebars [21][22][23], concrete piles for deep foundations [24][25], steel fasteners for timber connections [26][27], and bolted rock joints [28]. In this section, a model based on Timoshenko beam on elastic foundation with sign conventions as described in Figure 35 is considered in order to try to investigate the behaviour of the embedded steel profile.

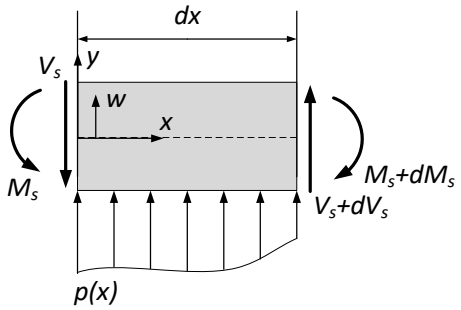


Figure 35: Convention for beam model on elastic foundation.

According to Timoshenko and Gere [29], the bending moment is related to the rotation of the beam $\theta_s(x)$ by the following expression :

$$M_s(x) = E_s I_s \frac{d\theta_s(x)}{dx} \tag{7}$$

with $E_s$, $I_s$ and $x$ being the Young's modulus, the moment of inertia of the embedded profile and the beam axis, respectively. The rotation of the beam is expressed by:

$$\theta_s(x) = -\frac{dw(x)}{dx} + \frac{1}{G_s A_s}\frac{dM_s(x)}{dx} \tag{8}$$

where $G_s$ and $A_s$ are the shear modulus and the section area of the embedded profile, respectively. The bending moment is also related to the pressure distribution as following:

$$\frac{d^2 M_s(x)}{dx^2} = -p(x) \tag{9}$$

Based on Winkler foundation, the pressure distribution on the embedded profile by the concrete $p(x)$ is assumed to be normal to the beam and directly proportional to the beam deflection $w(x)$:

$$p(x) = -kw(x) \tag{10}$$

where $k$ is the Winkler foundation modulus (see section 4.2.2). Combining Eqs. (7)-(10) gives a differential equation of bending moment as following:

$$\frac{d^4 M_s(x)}{dx^4} - 2\alpha_0 \frac{d^2 M_s(x)}{dx^2} + \beta_0 M_s(x) = 0 \tag{11}$$

with

$$\alpha_0 = \frac{k}{2G_s A_s} \tag{12}$$

$$\beta_0 = \frac{k}{E_s I_s} \tag{13}$$

The exact solution to this differential equation is

$$M_s(x) = e^{-\gamma x}[C_1 \cos(\varphi x) + C_2 \sin(\varphi x)] + e^{\gamma x}[C_3 \cos(\varphi x) + C_4 \sin(\varphi x)] \tag{14}$$

with

$$\gamma = \sqrt[4]{\beta_0}\cos\left[\frac{\arccos}{2}\left(\frac{\alpha_0}{\sqrt{\beta_0}}\right)\right] \tag{15}$$

$$\varphi = \sqrt[4]{\beta_0}\sin\left[\frac{\arccos}{2}\left(\frac{\alpha_0}{\sqrt{\beta_0}}\right)\right] \tag{16}$$

and, $C_1$, $C_2$, $C_3$ and $C_4$ are the constants of integration, dependent on the boundary conditions. The shear force $V_s(x)$ and the deflection of steel profile $w(x)$ are then obtained as :

$$\begin{aligned} V_s(x) = \frac{dM_s}{dx} = {} & \varphi e^{\gamma x}[C_2 \cos(\varphi x) - C_1 \sin(\varphi x)] + \varphi e^{-\gamma x}[C_4 \cos(\varphi x) - C_3 \sin(\varphi x)] \\ & + \gamma e^{\gamma x}[C_1 \cos(\varphi x) + C_2 \sin(\varphi x)] - \gamma e^{-\gamma x}[C_3 \cos(\varphi x) + C_4 \sin(\varphi x)] \end{aligned} \tag{17}$$

$$w(x) = \frac{1}{k}\frac{d^2M_s}{dx^2} = \frac{1}{k}\{2\gamma\varphi e^{\gamma x}[C_2\cos(\varphi x) - C_1\sin(\varphi x)] - \varphi^2 e^{-\gamma x}[C_3\cos(\varphi x) + C_4\sin(\varphi x)] - \varphi^2 e^{\gamma x}[C_1\cos(\varphi x) + C_2\sin(\varphi x)] - 2\gamma\varphi e^{-\gamma x}[C_4\cos(\varphi x) - C_3\sin(\varphi x)] + \gamma^2 e^{\gamma x}[C_1\cos(\varphi x) + C_2\sin(\varphi x)] + \gamma^2 e^{-\gamma x}[C_3\cos(\varphi x) + C_4\sin(\varphi x)]\} \quad (18)$$

Based on Figure 33a, the boundary conditions for the embedded profiles are:

$$M_s(0) = M_{Ed} \quad (19)$$
$$V_s(0) = V_{Ed}$$
$$M_s(1) = 0$$
$$V_s(1) = 0$$

The constants of integration are then obtained by solving Eqs. (19). However, in the case of the current configuration of the embedded profile (1-meter length), the following can be approximated:

$$C_1 = M_{Ed} \quad (20)$$
$$C_2 = \frac{(V_{Ed} + aM_{Ed})}{b}$$
$$C_3 = 0$$
$$C_4 = 0$$

4.2.2 *Defining Winkler foundation modulus*

The accuracy of the BEF model depends on the determination of the Winkler foundation modulus. In most studies, the value of this modulus is obtained empirically either from experiments or from numerical studies. However, the expression for the modulus in the case of embedded H-profiles is not available in the literature. In a first attempt in this paper, the Winkler foundation modulus is determined by considering the local deformation of the concrete based on a strut-and-tie model, as presented in Figure 36. The dimensions of the model are determined as following:

- The angle of the strut ($\alpha$) is fixed by the position of the stirrups.
- The height of the model ($h$) is fixed by the position of the inferior HA8 bending rebars.
- The width of the strut is determined with the expression below:

$$b_s = \left(\frac{r}{\tan\alpha} + r + 2t_f\right)\sin\alpha \quad (21)$$

It should be noted that the determination of the width of the strut by adding $2t_f$ is inspired from the approach for the area of equivalent T-stub in compression provided in EN 1993-1-8 [30].

- The length of the tie is computed by

$$L_0 = 2\frac{h}{\tan\alpha} + r\left(1 - \frac{1}{\tan\alpha}\right) + 2t_f + t_w \quad (22)$$

where $r$, $t_f$ and $t_w$ are the fillet radius, flange thickness and web thickness of the profile section, respectively.

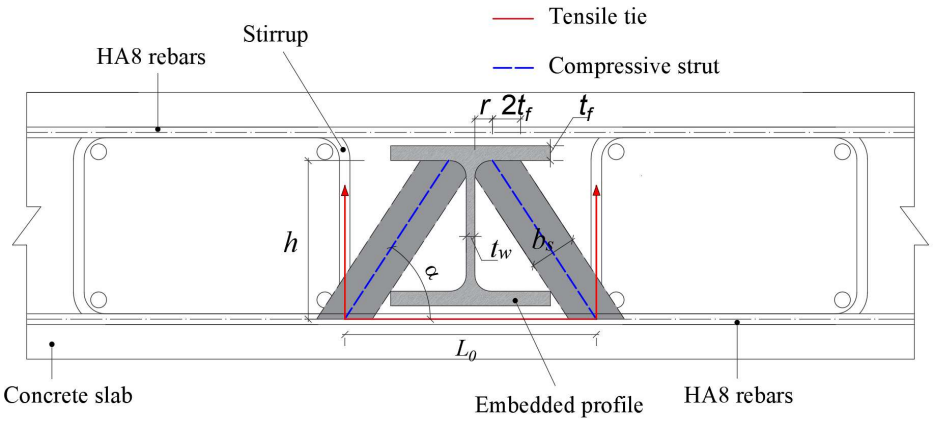


Figure 36:Strut-and-tie model for BEF model.

Consequently, in this model, the total displacement of the embedded profile is the sum of the displacements due to the deformability of the struts ($d_1$) and of the ties ($d_2$):

$$d = d_1 + d_2 \tag{23}$$

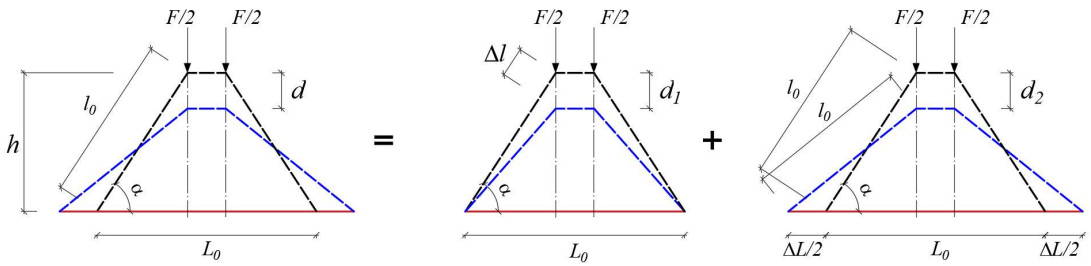


a. Total displacement b. Displacement due to struts c. Displacement due to ties

Figure 37: Total displacement of the strut-and-tie model.

The displacement due to the deformability of the struts can be determined in relation to the force as (see Figure 37):

$$d_1 = \frac{\Delta l}{\sin\alpha} = \frac{N_c l_0}{E_c A_{cs} \sin\alpha} = \frac{Fh}{2E_c b_s \sin^3\alpha} \tag{24}$$

where $E_c$, $A_{cs}$ and $N$ are the Young's modulus of the concrete, the section of the struts and the normal force in the strut, respectively. On the other hand, the displacement due to the deformability of the tie can be obtained in function of the elongation of the tie using the second-degree approximation, which gives:

$$d_2 = \frac{\Delta L}{2\tan\alpha} = \frac{N_t L_0}{2E_s A_{st} \tan\alpha} = \frac{FL_0}{4E_s A_{st} \tan^2\alpha} \tag{25}$$

In addition, the Winkler foundation modulus can be computed in relation to the force and the total displacement by

$$k = \frac{F}{d} \tag{26}$$

By combining Eqs. (23) to (26), we obtain

$$k = \frac{4E_c b_s E_s A_{st} \sin^3 \alpha}{E_c b_s L_0 \sin \alpha \cos^2 \alpha + 2E_s A_{st} h} \tag{27}$$

4.2.3 *Numerical application*

For a numerical application of the model, the values of parameters conforming to the experimental test are given in Table 3. Regarding the section of the tie ($A_{st}$), 8 HA-8mm rebars were placed inside the specimen within the first 400 mm from the concrete edge and after that one HA-8mm rebar each 100 mm of spacing (see Appendix A). In this first result, it is assumed to compute $A_{st}$ as following:

$$A_{st} = \frac{8 \times \frac{\pi \times 8^2}{4}}{400} = 1 \text{ mm}^2/\text{mm} \tag{28}$$

**Table 3: Values of parameters.**

| Parameter | $\alpha$ [°] | $h$ [mm] | $t_w$ [mm] | $t_f$ [mm] | $r$ [mm] | $G_s$ [GPa] | $A_s$ [Cm$^2$] | $E_s$ [GPa] | $E_c$ [GPa] | $I_s$ [MPa] | $A_{st}$ [mm$^2$/mm] |
|---|---|---|---|---|---|---|---|---|---|---|---|
| Value | 57 | 120 | 6.5 | 11 | 12 | 76.92 | 34 | 200 | 31 | 864 | 1 |

Using these values of the parameters, the width of the strut, the length of the tie and the Winkler foundation modulus are obtained and reported in **Table 4**. Afterwards, adopting the values of parameters given in **Table 3** and **Table 4**, the distributions of the shear force (Eq.(17)) and the bending moment (Eq.(14)) at different load levels of the embedded steel profile for the BEF model are provided in Figure 38 and Figure 39, respectively. In addition, these figures also include the distribution of the shear force and the bending moment on the concrete section obtained using Eqs. (3) and (4), respectively.

**Table 4: Values of Winkler foundation modulus.**

| Parameter | $b_s$ [mm] | $L_0$ [mm] | $k$ [N/m$^2$] |
|---|---|---|---|
| Value | 35 | 188.6 | 5.31E+09 |

It can be seen from these figures that the distributions of both shear forces and bending moments have similar trend between the analytical approach (BEF model) and the FE model until a load level of 20 kN (per profile). At this load level, the moment-deflection curves (see Figure 25) have a substantial change of slope, indicating permanent displacements of the system caused by local plastic deformation and damage of the concrete. Indeed, a linear elastic behaviour of the model of beam on elastic foundation is adopted. For a better estimation of the behaviour exceeding this point, an elasto-plastic behaviour of the spring should be adopted.

In addition, it should be noted that, in overall, the analytical approach overestimates the bending moment and the shear force on both the embedded H-profile and the concrete slab by around 20 percent at a load level of 10 kN and around 30 percent at a load level of 20 kN. It is important to remind that the results presented here are obtained by considering constant value of the Winkler foundation modulus along the length of the embedded profiles, whereas 8 HA-8mm rebars were placed inside the specimen only within the first 400 mm from the

concrete edge and after that one HA rebar at each 100 mm of spacing. The former is considered when computing the Winkler foundation modulus ($k$) in order to position for security, as the higher the value of $k$ is used the higher the embedded H-profile is solicitated, so as the concrete slab. This is confirmed by the results of the sensitivity study by changing the value of $k$ to $2k$ and $0.5k$, illustrated in Figure 40.

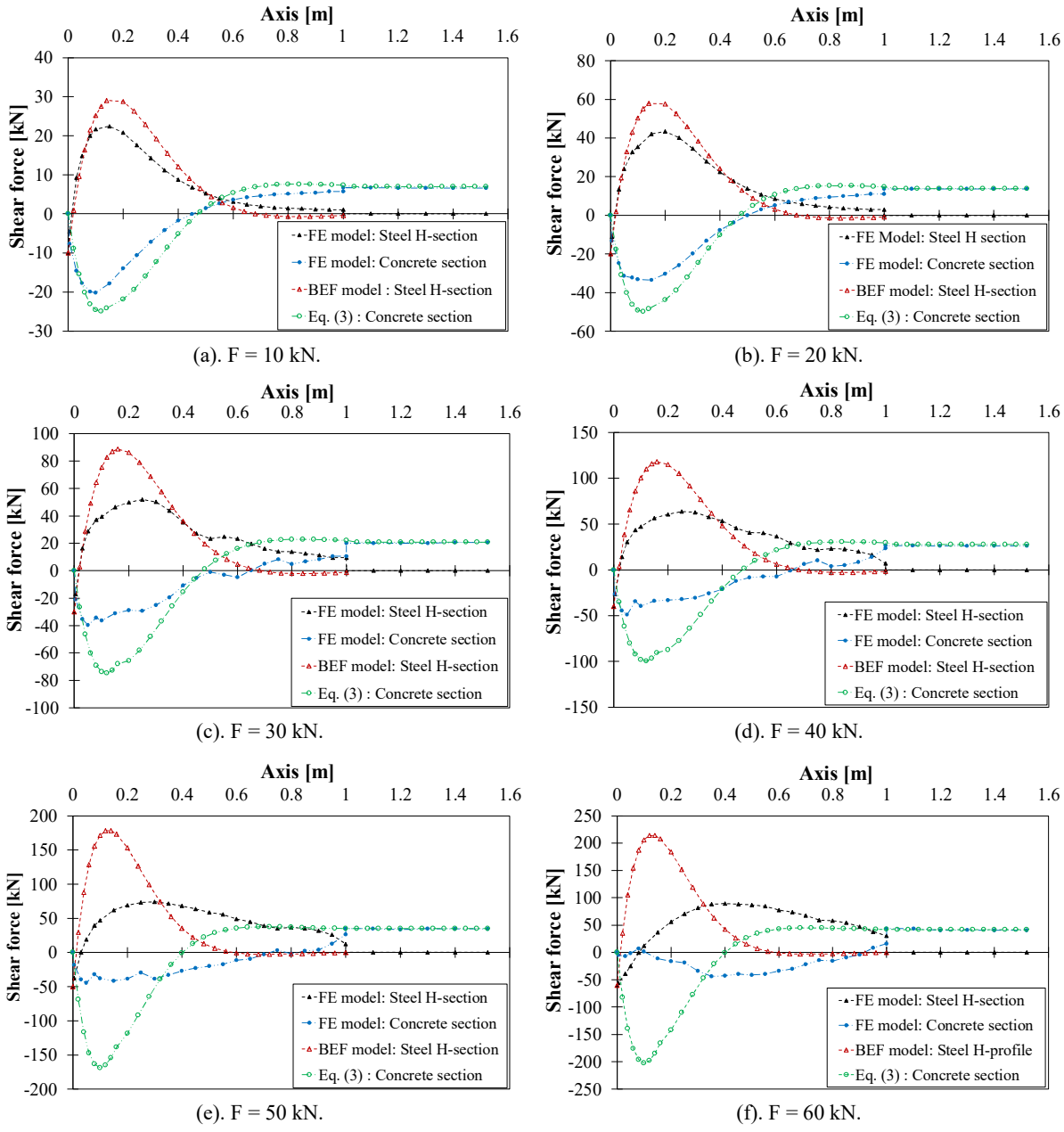


Figure 38: Comparison of distribution of shear force on steel and concrete sections at different load levels (per profile).

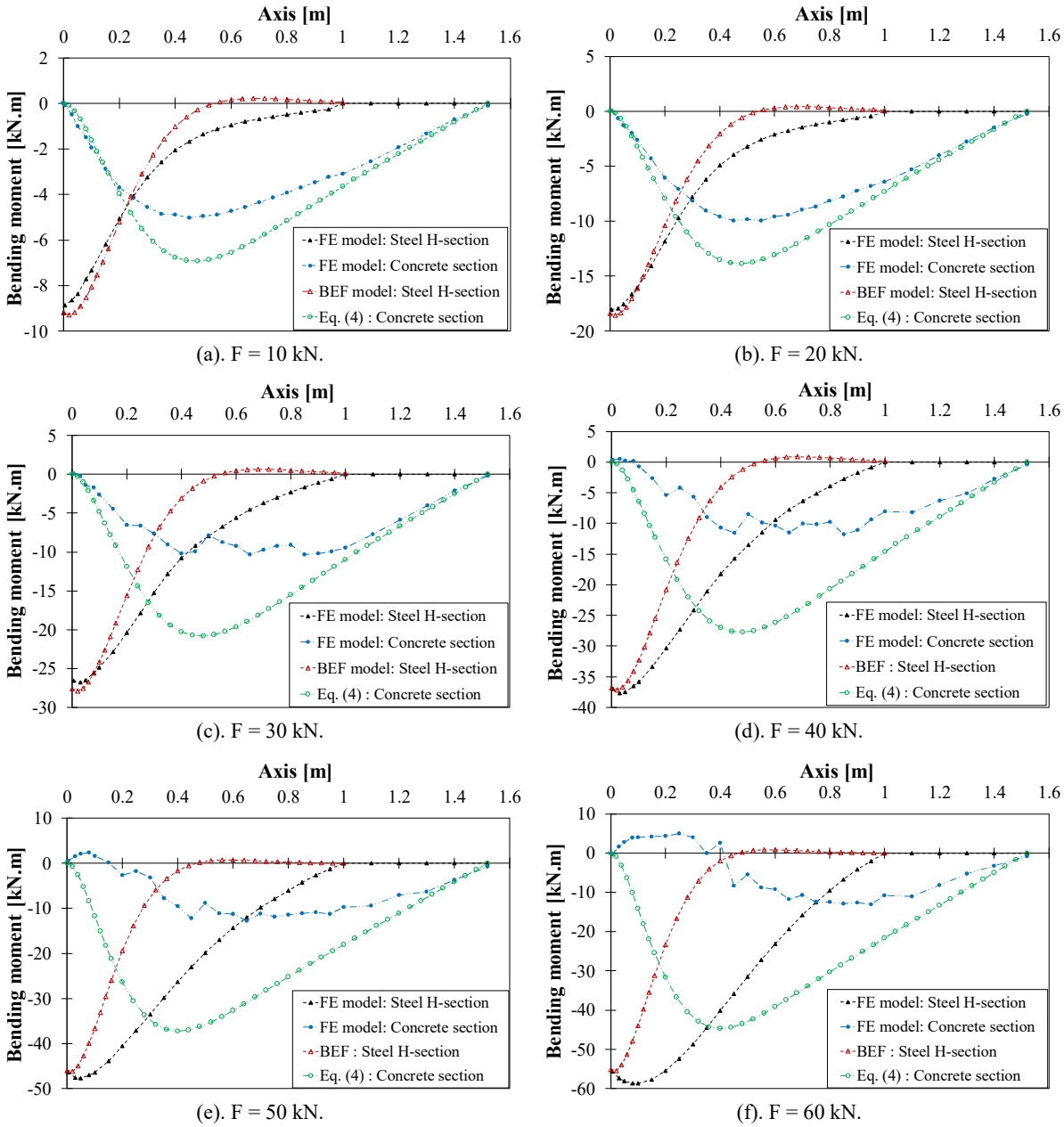


(a). F = 10 kN. (b). F = 20 kN.

(c). F = 30 kN. (d). F = 40 kN.

(e). F = 50 kN. (f). F = 60 kN.

Figure 39: Comparison of distribution of bending moment on steel and concrete sections at different load levels (per profile).

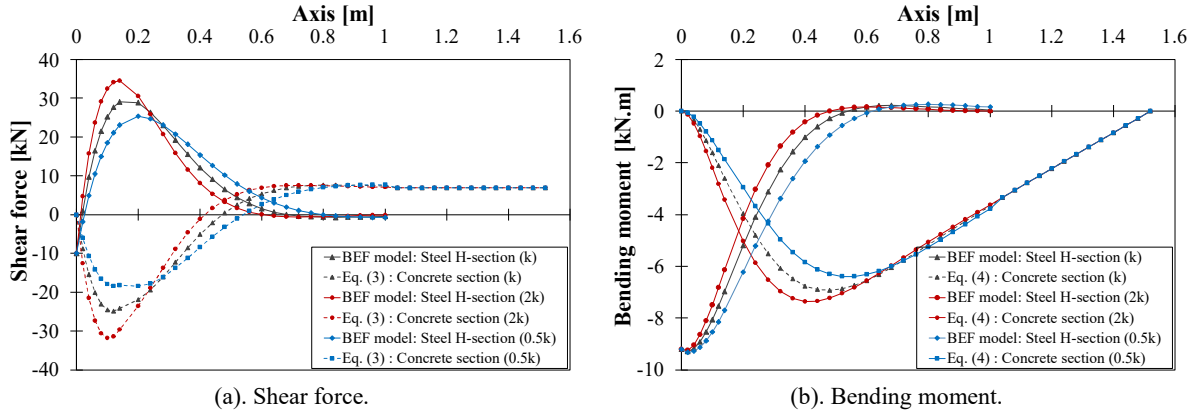


(a). Shear force. (b). Bending moment.

Figure 40: Sensitivity study on the value of the Winkler foundation modulus (at a load level of 10 kN).

In the design of the balcony-to-slab connection, the BEF model can be adopted to determine the distributions of the bending moments and the shear forces in the embedded steel profiles, as well as in the concrete. The design needs to verify that these bending moments and shear forces do not exceed their elastic limits, respectively.

## 5. Conclusion

This paper presents experimental and numerical investigations on the behaviour of long embedded H-profile balcony-to-slab connection. A reduced large-scale experimental test on the system has been carried out in order to determine the bearing capacity, the deformation capacity, the cracking patterns, the failure mode of the system and the deformation distribution as well as the bending distribution of the embedded profile. For a better understanding of the load transfer mechanism of the connection system, a full 3D FE simulation of the experimental test has been performed in ABAQUS/Explicit and validated against experimental results. Based on the useful information obtained from the validated FE model, a practical design approach based on Timoshenko beam on elastic foundation is investigated considering the local deformation of the concrete based on a strut-and-tie model. The following results are obtained from this study:

- The experimental results show inclined cracks on the concrete slab, initiated from the extremities of the top flange of embedded H-profiles. The failure was governed by cracks that link these inclined cracks to the lateral cracks. In addition, compared to the experimental results, the expressions for the ultimate shear and bending capacities derived from the assumed stress distribution by Mattock and Gaafar [4] are not satisfying for the case of the present embedded H-profile balcony-to-slab connection.
- The FE simulation of the experimental test has been successfully developed and validated against experimental data. A good agreement is obtained between the results obtained from the FE model and those from the experimental test, such as the moment-deflection curves of the cantilever beams and of the concrete slab, the distribution of the bending moment along the axis of the embedded H-profile, and the evolution of the strains on the embedded H-profile in function of the bending moment at different positions along the axis. The FE model is also able to accurately reproduce the observations made in the experimental tests such as the inclined cracks, the flexural cracks, the inclination angles of the cracks and the failure mode. At last, the distributions of the shear force and of the bending moment on the composite cross-section agree well with the results using the classic beam theory.
- Deduced from the results of the validated FE model, it is possible to assume that the shear force applied to the composite cross-section is a sum of the shear forces applied to the embedded H-profile and the concrete slab cross-sections. The same also applies to the bending moments.
- With the proposed strut-and-tie model for estimating the Winkler foundation modulus, the BEF model is able to provide results that reasonably match with those from the FE model in the linear elastic range, but deviate in the nonlinear range. Even so, the model is conformed to the conventional method for structural analysis based on the elastic theory.

Clearly, these conclusions are based on a relatively limited number of tests and numerical studies. In the future, it is interesting to perform additional experimental tests and a parametric study using the validated FE model in order to investigate the influence of important parameters on the behaviour of the connection system.

## Acknowledgements

The authors gratefully acknowledge financial support by the ANR (Agence Nationale de la Recherche, Paris) and INGENOVA with a grant number ANR-15-LCV2-0003 through the LABCOM ANR B-Hybrid project.

**Appendix A:** details of the reinforcement rebars of the test specimen.

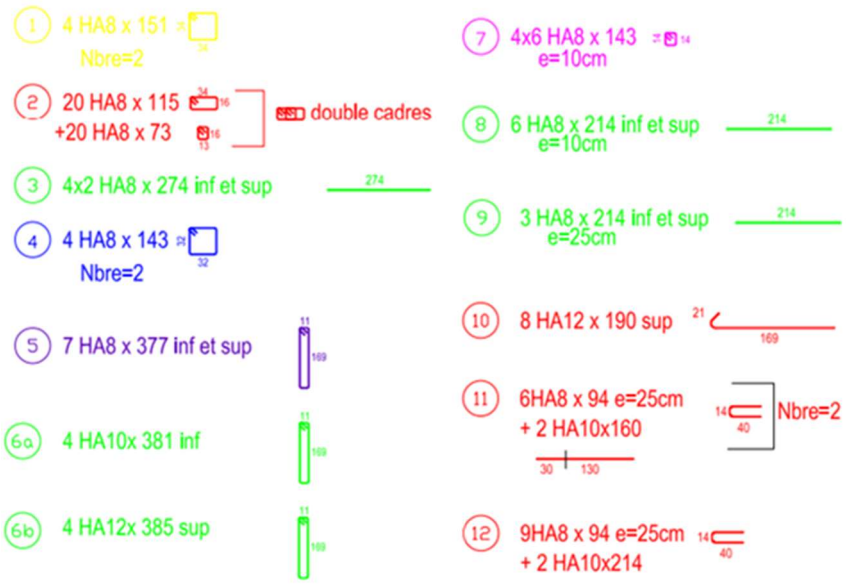


Figure A1: Nomenclature.

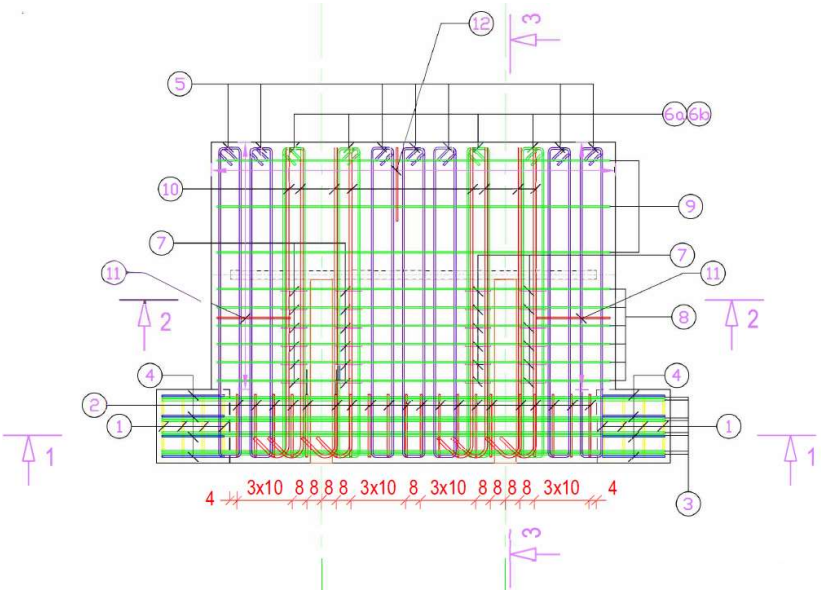


Figure A2: Plane view.

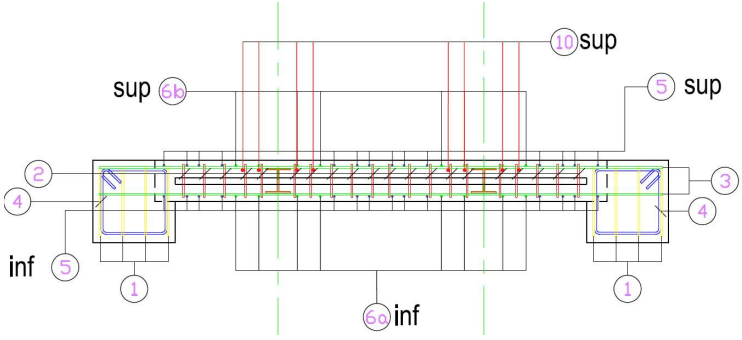


Figure A3: Cut 1-1.

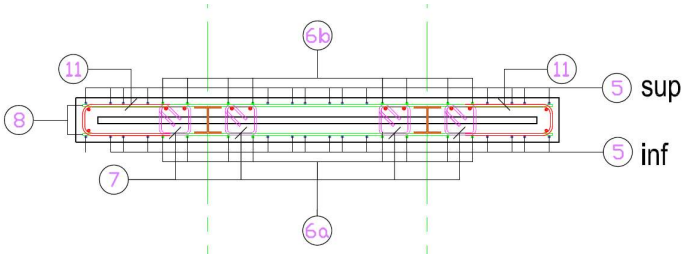


Figure A4: Cut 2-2.

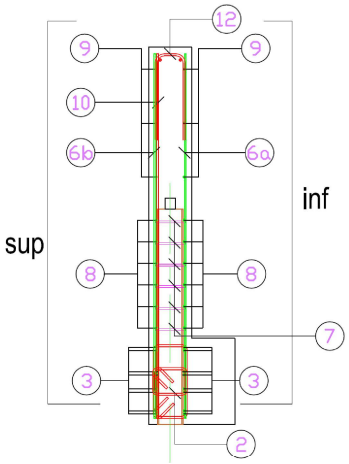




Figure A5: Cut 3-3.

**Appendix B:** details of the steel profiles of the test specimen.

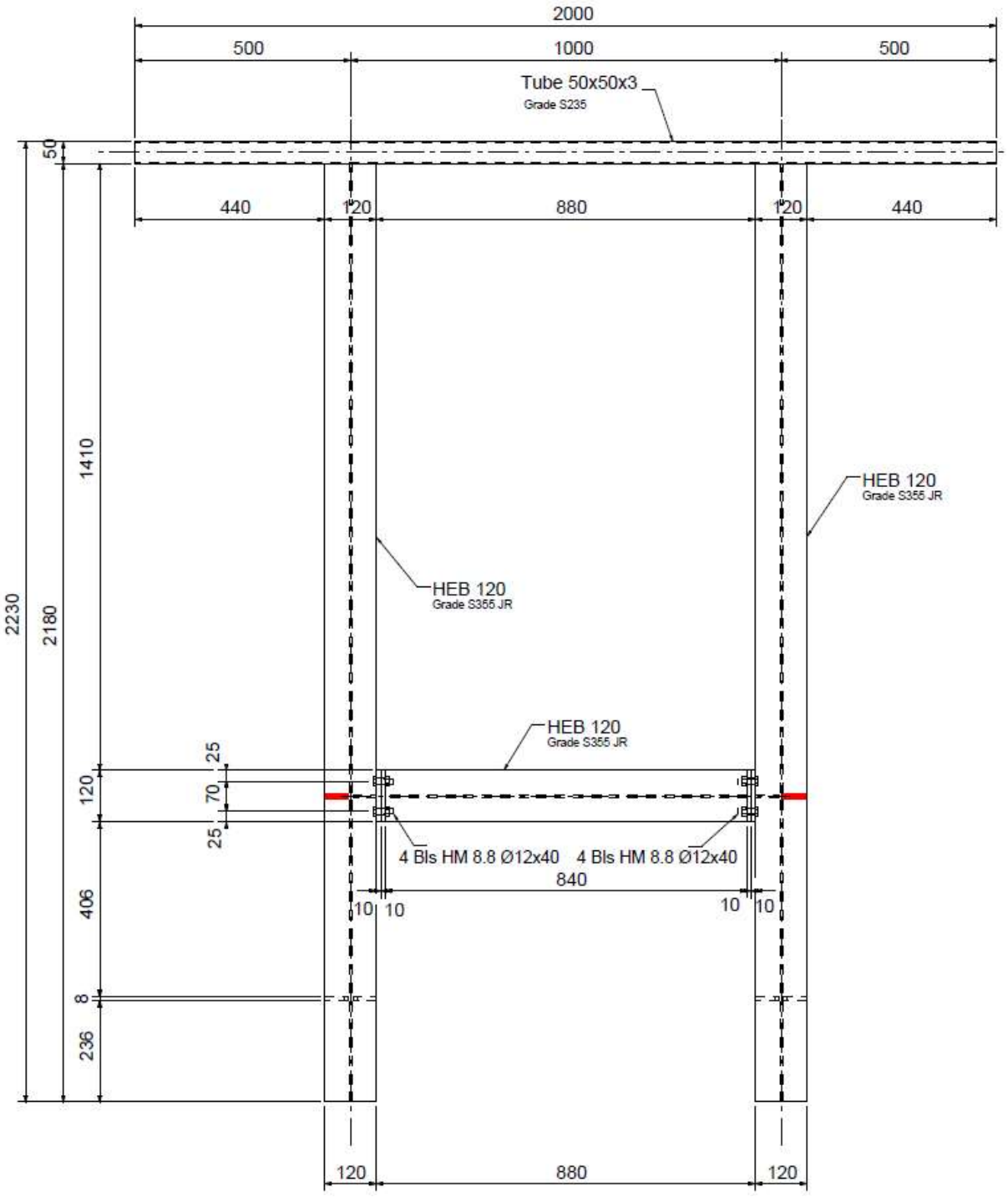


Figure B1: Dimensions of steel profiles of the test specimen.

## References


[1] C. H. Raths, Embedded structural steel connections, PCI Committee on Connection Details, PCI Manual on Design of Connections for Precast Prestressed Concrete, Prestressed Concrete Institute, Chicago, (1974) 104–112.

[2] J. L. Clarke, R. M. Symmons, Test on Embedded Steel Billets for Precast Concrete Beam–Column Connection. Technical Report No. 42, vol. 523. Cement and Concrete Association, London, (1978): 12–24.

[3] K. Marcakis, D. Mitchell, Precast concrete connections with embedded steel members. Prestressed Concrete Institute Journal, 25(4) (1980): 88–116.

[4] A. H. Mattock, G. H. Gaafar, Strength of embedded steel sections as brackets. ACI Journal, 79(2) (1982): 83–93.

[5] B. Gong, B. M. Shahrooz, Steel-concrete composite coupling beams — behaviour and design. Engineering Structures, 23 (2001): 1480–1490.

[6] B. M. Shahrooz, M. E. Remmetter, F. Qin, Seismic design and performance of composite coupled walls. Journal of Structural Engineering, 119(11) (1993): 3291-3309.

[7] K. A. Harries, B. Gong, B. M. Shahrooz, Behavior and design of reinforced concrete, steel, and steel-concrete coupling beams. Earthquake Spectra, 16(4) (2000) 775-799.

[8] W.S. Park, H. D. Yun, Seismic behaviour of steel coupling beams linking reinforced concrete shear walls. Engineering Structures, 27 (2005): 1024-1039.

[9] S. El-Tawil, K. A. Harries, P. J. Fortney, B. M. Shahrooz, Y. Kurama, Seismic design of hybrid coupled wall systems: State of the art. Journal of Structural Engineering, 136(7) (2010): 755-769.

[10] S. El-Tawil, P. J. Fortney, K. A. Harries, B. M. Shahrooz, Y. Kurama, M. Hassan, X. Tong, Recommendations for seismic design of hybrid coupled wall systems. American Society of Civil Engineers (2009).

[11] ANSI/AISC 341-10, Seismic Provisions for Structural Steel Buildings. American Institute of Steel Construction, Chicago, Illinois, 2010.

[12] G. Corley, N. Hawkins, Shearhead reinforcement for slabs. ACI Structural Journal (1968) : 811-824.

[13] M. A. Eder, R. L. Vollum, A. Y. Elghazouli, T. Abdel-Fattah, Modelling and experimental assessment of punching shear in flat slabs with shearheads. Engineering Structures, 32 (2010): 3911-3924.

[14] C. H. Lee, J. W. Kim, J. G. Song, Punching shear strength and post-punching behavior of CFT column to RC flat plate connections. Journal of Constructional Steel Research, 64(4) (2008): 418-428.

[15] D. V. Bompa, A. Y. Elghazouli, Structural performance of RC flat slabs connected to steel columns with shear heads. Engineering Structures 117 (2016): 161-183.

[16] Abaqus documentation, version 6.14., Dassault system 2014.

[17] NF EN12390-3, Testing Harden Concrete: Compressive Strength of Test Specimens, AFNOR - French standard institute, 2003.

[18] NF EN ISO 6892-1, Metallic Materials - Tensile Testing - Part 1: Method of Test at Room Temperature, AFNOR - French standard institute, 2009.

[19] EN1994-1-1, Eurocode 4: Design of Composite Steel and Concrete Structures–Part 1.1: General Rules and Rules for Buildings, European Committee for Standardization, Brussels, 2010.

[20] B. Alfarah, F. López-Almansa, S. Oller, New methodology for calculating damage variables evolution in plastic damage model for rc structure, Eng. Struct. 132 (2017)70–86.

[21] A. R. Moradi, M. Soltani, A. A. Tasnimi, A simplified constitutive model for dowel action across RC cracks. J Adv Concr Technol. 2012;10(8):264–277.

[22] E.-A. Bilal, Behavior of beams with dowel action. Engineering Structures 29 (2007) 899–903.

[23] P. Soroushian, K. Obaseki, M. C. Rajos, Bearing strength and stiffness of concrete under reinforcing bars. ACI Materials Journal, 84 (3) (1987): 179-184.

[24] B. B. Broms, Lateral Resistance of Piles in Cohesive Soils. Journal of the Soil Mechanics and Foundations Division, 90(2)(1964): 123-156.

[25] K. Terzaghi, Evaluation of coefficients of subgrade reaction. Geotechnique 5(4)(1955): 297-326.

[26] H. Tao, H. Yang, G. Ju, B. Shi, Elastic stiffness of timber joints with dowel-type fasteners and slotted-in steel plate based on the theory of beam on elastic foundation. Construction and Building Materials, 294(2021): 123569.

[27] Y. D. Santis, M. Fragiacomo, Timber-to-timber and steel-to-timber screw connections: Derivation of the slip modulus via beam on elastic foundation model. Engineering structures 244(2021): 112798.

[28] S. Ma, Z. Zhao, J. Shang, An analytical model for shear behaviour of bolted rock joints. International Journal of Rock Mechanics and Mining Sciences 121(2019): 104019.

[29] S. P. Timoshenko, J. M. Gere, Theory of elastic stability. McGraw-Hill Book Company, New York, USA., 1963.

[30] Eurocode 3: Design of steel structures – Part 1-8: Design of joints. NF EN 1993-1-8:2010-12.